SOLID STATE ELECTRONICS LABORATORY

STANFORD ELECTRONICS LABORATORIES
DEPARTMENT OF ELECTRICAL ENGINEERING
STANFORD UNIVERSITY · STANFORD, CA 94305

SU-SEL-78-014

THE RECOMBINATION VELOCITY AT III-V COMPOUND HETEROJUNCTIONS WITH APPLICATIONS TO $Al_xGa_{1-x}As$-$GaAs_{1-y}Sb_y$ SOLAR CELLS

(NASA-CR-157181) THE RECOMBINATION VELOCITY AT III-V COMPOUND HETEROJUNCTIONS WITH APPLICATIONS TO Al (x) Ga (1-x) As-GaAs (1-y) Sb (y) (Stanford Univ.) 78 p HC A05/MF A01 CSCL 10A G3/44
N78-25544
Unclas
21377

by

Jung-Soon Kim

May 1978

Technical Report No. 5127-1

Prepared under

National Aeronautics and Space Administration
Grant NSG-1201

SU-SEL-78-014

THE RECOMBINATION VELOCITY AT III-V COMPOUND HETEROJUNCTIONS WITH APPLICATIONS TO $Al_xGa_{1-x}As$-$GaAs_{1-y}Sb_y$ SOLAR CELLS

by

Jung-Soon Kim

May 1978

Technical Report No. 5127-1

Prepared under

National Aeronautics and
Space Administration
Grant NSG-1201

Solid-State Laboratory
Stanford Electronics Laboratories
Stanford University   Stanford, California

ABSTRACT

Interface recombination velocity in $Al_xGa_{1-x}As$-GaAs and $Al_{0.85}Ga_{0.15}As$-$GaAs_{1-y}Sb_y$ heterojunction systems is studied as a function of lattice mismatch. The results are applied to the design of highly efficient III-V heterojunction solar cells.

A horizontal liquid-phase epitaxial growth system was used to prepare p-p-p and p-p-n $Al_xGa_{1-x}As$-$GaAs_{1-y}Sb_y$-$Al_xGa_{1-x}As$ double-heterojunction test samples with specified values of x and y. Samples were grown at each composition, with different GaAs and GaAsSb layer thicknesses.

A method was developed to obtain the lattice mismatch and lattice constants in mixed single crystals grown on (100) and (111)B oriented GaAs substrates. In the AlGaAs system, elastic lattice deformation with effective Poisson ratios $\nu_{eff}(100) = 0.312$ and $\nu_{eff}(111B) = 0.190$ was observed. The lattice constant $a_o(Al_xGa_{1-x}As) = 5.6532 + 0.0084x$ Å was obtained at 300 K which is in good agreement with Vegard's law. In the GaAsSb system, although elastic lattice deformation was observed in (111)B-oriented crystals, misfit dislocations reduced the Poisson ratio to zero in (100)-oriented samples. When $a_o(GaSb) = 6.0959$ Å was assumed at 300 K, both (100) and (111)B oriented GaAsSb layers deviated only slightly from Vegard's law. Both (100) and (111)B zero-mismatch $Al_{0.85}Ga_{0.15}As$-$GaAs_{1-y}Sb_y$ layers were grown from melts with a weight ratio of $W_{Sb}/W_{Ga} = 0.13$ and a growth temperature of 840 to 820°C. The corresponding Sb compositions were $y = 0.015$ and 0.024 on (100) and (111)B orientations, respectively. This occurs because of a fortuitous variation in the Sb distribution coefficient with orientation.

Interface recombination velocity was estimated from the dependence of the effective minority carrier lifetime on double-heterojunction spacing, using either optical phase-shift or electroluminescence time-decay techniques. The recombination velocity at a (100) interface was reduced from (2 to 3) $\times 10^4$ for $y=0$ to (6 to 7) $\times 10^3$ cm/sec for lattice-matched $Al_{0.85}Ga_{0.15}As-GaAs_{0.985}Sb_{0.015}$. Although this reduction is slightly less than that expected from the exponential relationship between interface recombination velocity and lattice mismatch as found in the AlGaAs-GaAs system, solar cells constructed from such a combination of materials should have an excellent spectral response to photons with energies over the full range from 1.4 to 2.6 eV. Similar measurements on a (111)B oriented lattice-matched heterojunction produced somewhat larger interface recombination velocities.

CONTENTS

ILLUSTRATIONS

ILLUSTRATIONS (Cont)

TABLES

SYMBOLS

a_f	lattice constant of epitaxial layer (Å)
$a_f^{\parallel}$	strained lattice constant of epitaxial layer parallel to substrate surface (Å)
$a_f^{\perp}$	strained lattice constant of epitaxial layer perpendicular to substrate surface (Å)
a_o	lattice constant (Å)
a_s	lattice constant of substrate (Å)
C	real quantity
C'	real quantity
D	distribution coefficient
D_n	diffusion constant of electron minority carriers (cm^2/sec)
d	double-heterojunction spacing (μm)
E	Young's modulus
E_f	Fermi energy (eV)
E_g	band-gap energy (eV)
G_s	electron-hole generation rate (pairs/cm^3-sec)
I_s	electron beam-induced current (nA)
L_n	minority carrier (electron) diffusion length (μm)
L_p	minority carrier (hole) diffusion length (μm)
S	interface recombination velocity (cm/sec)
T_G	growth temperature (°C)
W_{Al}	weight of Al in melt (gm)
W_{Ga}	weight of Ga in melt (gm)
W_{Sb}	weight of Sb in melt (gm)
x	mole fraction of AlAs in AlGaAs ternary compound
y	mole fraction of GaSb in GaAsSb ternary compound

α	thermal-expansion coefficient (1/°C)
Δa	strain-free lattice-constant difference between epitaxial layer and substrate (Å)
Δn	excess minority carrier (electron) density (cm^{-3})
$\Delta\bar{n}$	average excess electron minority carrier density (cm^{-3})
$\Delta a^{\perp}$	perpendicular strained lattice-constant difference between epitaxial layer and substrate (Å)
$\Delta a^{\parallel}$	parallel strained lattice-constant difference between epitaxial layer and substrate (Å)
$\Delta\theta_B$	angular difference caused by difference of lattice spacing normal to the substrate surface (sec)
$\Delta\theta_1$	separation angle between $K_{\alpha 1}$ peaks of substrate and epitaxial layer (sec)
$\Delta\theta_2$	same quantity as above, measured after rotating the crystal by 180° around the normal to the substrate surface (sec)
$\epsilon^{\perp}$	strain perpendicular to substrate surface
$\epsilon^{\parallel}$	strain parallel to substrate surface
θ	phase difference (degree)
θ_B	Bragg's angle (degree)
λ	wavelength (Å)
ν_{eff}	effective Poisson ratio
ξ	normalized interface recombination velocity
$\sigma^{\perp}$	stress perpendicular to substrate surface
$\sigma^{\parallel}$	stress parallel to substrate surface
τ_{eff}	effective minority carrier lifetime (nsec)
τ_o	bulk lifetime (nsec)
ω	angular frequency of a pulsed laser

ACKNOWLEDGMENT

I wish to express my deep gratitude to Professor Gerald L. Pearson for his guidance and encouragement throughout this research. I also extend my sincere appreciation to Professors Richard H. Bube and Richard M. Swanson for reading this manuscript.

The X-ray measurements of Dr. Tom R. Cass of the Hewlett-Packard Laboratory and suggestions regarding crystal growth and lifetime measurements of Drs. Don R. Scifres and Robert D. Burnham are gratefully acknowledged, as are the valuable and stimulating discussions with them. Special thanks go to Dr. Robert M. White of the Xerox Palo Alto Research Center for permission to use their lifetime measuring equipment. The continued interest and encouragement of Dr. James A. Hutchby are appreciated.

This work was supported by the National Aeronautics and Space Administration Langley Research Center under Research Grant NSG-1201.

I would like to thank my wife, Eun-Young, for her unselfish patience and support and my parents, Mr. and Mrs. Sun Jip Kim, for their unremitting encouragement.

Chapter I

INTRODUCTION

Although theoretical studies [1,2] have demonstrated that GaAs should be one of the best materials for constructing solar cells, the efficiency of the early p-n junction GaAs solar cells was poor. The reasons for this inefficiency are that this direct band-gap material requires the p-n junction to be less than 1 μm from the surface and that the GaAs-air interface has a large surface recombination velocity of approximately 10^6 cm/sec.

These difficulties were overcome during the early 1970's by growing thin (p)$Al_xGa_{1-x}As$ layers on the surfaces of p-n junction GaAs solar cells. Although this window layer is opaque to high-energy photons (>2.0 eV), the heterojunction confines the photon-generated electrons within the (p)GaAs layer, thereby providing a low-interface recombination velocity that greatly increases the efficiency compared to that of a simple GaAs cell; efficiencies up to 21 percent at AM1.4 have been reported [3].

Even after this improvement, efficiency was still far from the theoretical value (~ 27 percent), perhaps as a result, in part, of lattice mismatch at the heterojunction interface. The lattice constant a_o of GaAs, AlAs, and GaSb single crystals at room temperature is 5.6532, 5.6622, and 6.0959 Å, respectively [4]. The mismatch at a GaAs-AlAs heterojunction is thus 0.16 percent and, if Vegard's law is obeyed, the mismatch at a GaAs-$Al_xGa_{1-x}As$ heterojunction is 0.16x percent. This mismatch is small in comparison to other known heterojunction systems; however, it is large enough to produce finite interface recombination velocities. The fact that this lattice mismatch can be eliminated by adding Sb to GaAs led to the measurement of recombination velocity at a lattice-matched AlGaAs-GaAsSb interface as well as at $Al_xGa_{1-x}As$-GaAs interfaces. Electroluminescent time-decay and optical phase-shift techniques were employed to determine the heterojunction-interface recombination velocities, and a double-crystal X-ray diffractometer was used to measure precise heterojunction lattice mismatch. Based on these data, $Al_xGa_{1-x}As$-$GaAs_{1-y}Sb_y$ solar cells can be optimized to achieve maximum efficiency.

Methods to obtain the interface recombination velocity are theoretically analyzed in Chapter II, and relevant sample structures and techniques for measuring effective lifetimes are discussed. Liquid phase epitaxial (LPE) growth techniques, including melt and substrate preparation and procedures for growing double-heterojunction (DH) samples, are described in Chapter III, followed by characterization of the grown layers. In Chapter IV, theoretical relations are derived to determine both strained and strain-free lattice mismatch between the epitaxial layer and the substrate, assuming only two simplified lattice defects (elastic lattice deformation and misfit dislocations). Experimental results from AlGaAs-GaAs and GaAsSb-GaAs interfaces are described in detail. Schematics of the apparatus employed to evaluate effective lifetimes using both optical phase-shift and electroluminescent (EL) time-decay measurement techniques are presented in Chapter V. Interface recombination velocities are evaluated from best-curve fits based on heterojunction spacing and measured effective lifetime for fixed bulk lifetime and minority carrier diffusion length. Recombination velocities, $S = (2 \text{ to } 3) \times 10^4$ and $(6 \text{ to } 7) \times 10^3$ cm/sec, were achieved at (100) $Al_{0.85}Ga_{0.15}As$-GaAs and lattice-matched $Al_{0.85}Ga_{0.15}As-GaAs_{0.985}Sb_{0.015}$ heterojunction interfaces, respectively. A summary of the significant aspects of this research and suggestions for future study are included in Chapter VI.

Chapter II

INTERFACE RECOMBINATION VELOCITY

Interface recombination velocity can be determined from the dependence of the minority carrier lifetime on heterojunction spacing of symmetrical double-heterostructure (DH) samples. This is analogous to a semiconductor slab confined by two surfaces of equal recombination velocity [5,6,7].

A. Theory

A symmetrical $Al_xGa_{1-x}As$-$GaAs_{1-y}Sb_y$ DH sample is illustrated in Fig. 1, where Al composition x and recombination velocity S are assumed to be the same at both heterojunctions. It is also assumed that (1) the sample is an infinite slab of extrinsic p-type, (2) external surface excitation is uniform throughout the illuminated heterojunction interface, and (3) the electron-hole pairs are generated only near the interface. This is true when the sample is excited by laser light which has a photon energy larger than the band gap of the $GaAs_{1-y}Sb_y$ layer and smaller than

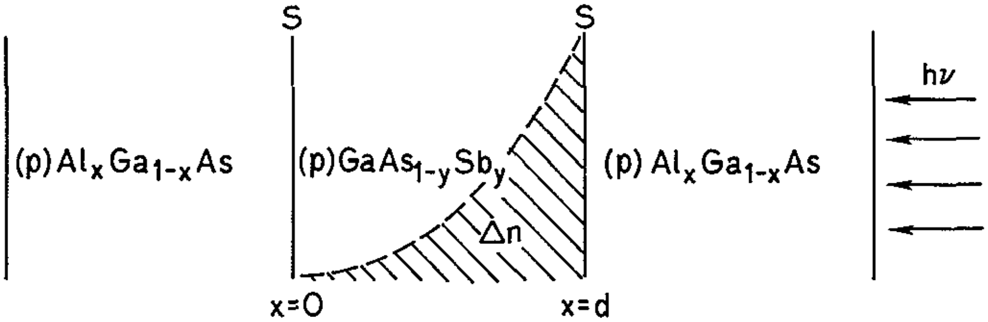

Fig. 1. ONE-DIMENSIONAL DIAGRAM OF A SYMMETRICAL (p)AlGaAs-(p)GaAsSb DH INFINITE SLAB.

that of the $Al_xGa_{1-x}As$ layer. In addition, low-level excitation is assumed so that the injected minority carrier (electron, in this case) density Δn is much less than the background hole density. Possible effects caused by light reabsorption within the recombination region are neglected in this analysis.

The continuity equation of minority carriers for the steady-state case and the relations for the two boundary conditions at the interfaces are

$$D_n(d^2\Delta n/dx^2) - \Delta n/\tau_o = 0 \tag{2.1}$$

and

$$-D_n(d\Delta n/dx)_{x=d} + G_s = S(\Delta n)_{x=d} \tag{2.2a}$$

$$D_n(d\Delta n/dx)_{x=0} = S(\Delta n)_{x=0} \tag{2.2b}$$

where D_n is the diffusion constant of the minority carriers and τ_o is the bulk lifetime in the p-type semiconductor. These quantities are related to the bulk-electron diffusion length by $L_n = (D_n\tau_o)^{1/2}$. The generation rate G_s is included in the boundary condition [Eq. (2.2a)] rather than in the continuity equation, for simplicity. In this analysis, trapping was not considered.

From the solution of Eq. (2.1), the excess minority carrier density is [5,6]

$$\Delta n(\tau) = (G_s/d)(d/2L_n)^2 \times \frac{(d/L_n)\cosh(\tau/L_n) + (Sd/D_n)\sinh(\tau/L_n)}{\left\{(Sd/2D_n)^2 + (d/2L_n)^2\right\}\sinh(d/L_n) + (Sd/2D_n)(d/L_n)\cosh(d/L_n)} \tag{2.3}$$

With the following definitions,

$$\Delta\bar{n} = (1/d) \int_0^d n(x)\, dx = (G_s/d)\, \tau_{eff}$$

$$\xi = SL_n/D_n$$

Eq. (2.3) can be simplified to

$$(\tau_{eff}/\tau_o) = \frac{\sinh (d/L_n) + \left(\cosh (d/L_n) - 1\right)}{(\xi^2 + 1) \sinh (d/L_n) + 2\xi \cosh (d/L_n)} \qquad (2.4)$$

where

$\Delta\bar{n}$ = average injected minority carrier density

τ_{eff} = effective minority carrier lifetime

ξ = normalized interface recombination velocity

When $d \ll L_n$ and $\xi \ll 1$, Eq. (2.4) reduces to $(1/\tau_{eff}) = (1/\tau_o) + (2S/d)$. Figure 2 is a plot of the normalized effective minority carrier lifetime τ_{eff}/τ_o as a function of the normalized heterojunction spacing d/L_n for various values of ξ.

Figure 2 implies that, if τ_o and L_n are known, the interface recombination velocity can be determined by curve fitting [8,9] from the measurement of the effective minority carrier lifetime and heterojunction spacing. It also shows a reduction of τ_{eff} with decreasing values of d.

B. Measuring Techniques

As discussed above, when τ_o and L_n are known, the interface recombination velocity can be obtained from the dependence of effective minority carrier lifetime on the heterojunction spacing of symmetrical

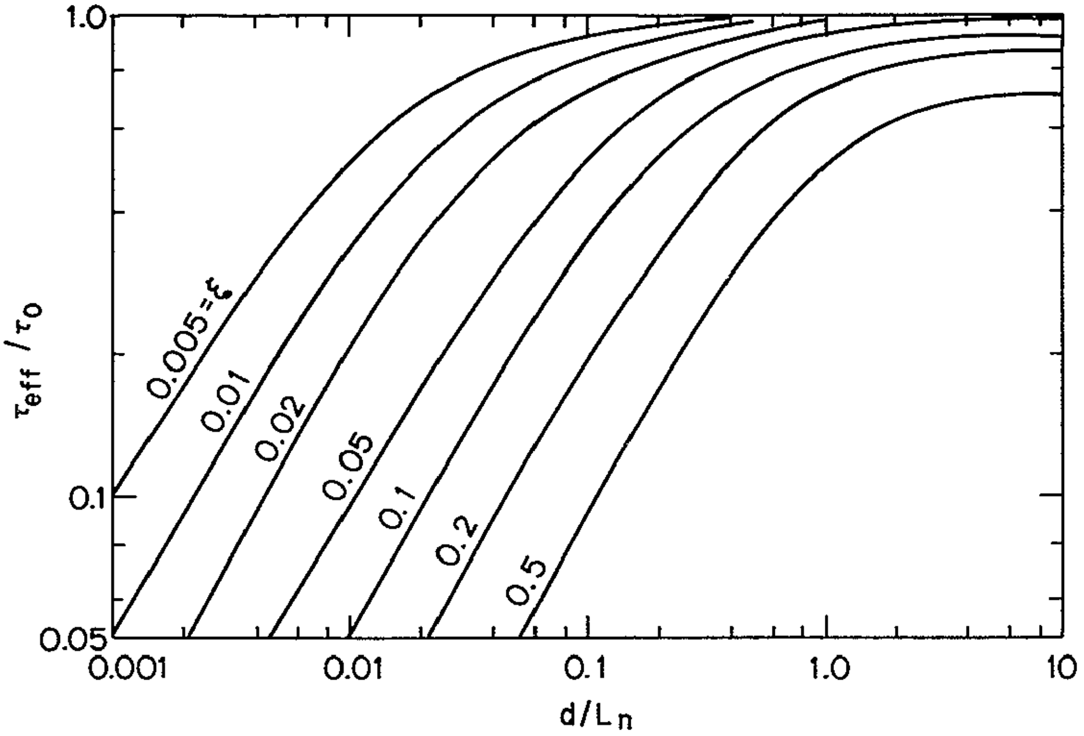

Fig. 2. NORMALIZED EFFECTIVE MINORITY CARRIER LIFETIME (τ_{eff}/τ_o) AS A FUNCTION OF HETEROJUNCTION SPACING (d/L_n). The independent parameter is the interface recombination velocity ξ.

DH samples. The next problem is to select measuring techniques that are available and feasible among the existing instruments for determining effective minority carrier lifetimes.

Several available techniques include electroluminescent (EL) time decay [6,7,8], pulsed reverse-bias recovery [10,11], current decay from pulsed laser beams [12], and optical phase shift [13,14]. Among these, EL time-decay and optical phase-shift techniques were chosen, and the p-p-p and p-p-n DH samples were used for the optical and EL measurements, respectively. Effective minority carrier lifetime can be directly determined from EL time-decay measurements but only indirectly from optical phase-shift measurements (see Chapter V for additional details). The heterojunction spacing d was determined with a conventional optical microscope after staining the cleaved edges of the samples.

C. Sample Structure

Figure 3 presents energy-band diagrams of the test samples. Figure 3a is the energy-band diagram of a p-p-p DH sample, and Figs. 3b and 3c

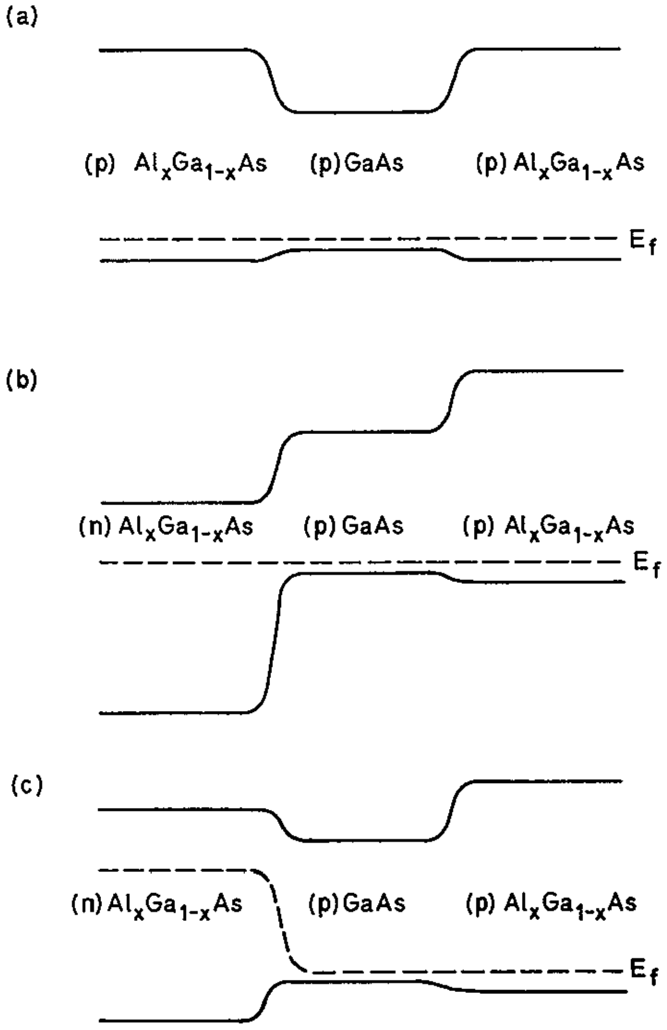

Fig. 3. ENERGY-BAND DIAGRAMS OF DH SAMPLES. (a) p-p-p DH sample, (b) p-p-n DH diode under no bias, and (c) p-p-n DH diode under forward bias.

apply to unbiased and biased p-p-n DH diodes. A similarity can be observed between (a) and (c), especially in the p-p-n DH diodes when the (p)GaAs [or (p)GaAsSb] layers were more heavily doped than the (n)AlGaAs layers. In this case, it can be assumed that the depletion region (approximately 0.1 μm in thickness) at the p-n junction is located inside the (n)AlGaAs layer and that the electron-hole pair recombination rate caused by space charge is thus minimized.

DH samples with various heterojunction spacings (0 to 15 μm) were prepared by liquid phase epitaxial (LPE) growth techniques on the GaAs substrates. Details regarding LPE crystal growth are discussed in Chapter III. In this study, the Al composition x of the $Al_xGa_{1-x}As$ layers was set at $x = 0.85$. The corresponding band-gap energy is ~2.05 eV. Although attempts were made to grow $Al_xGa_{1-x}As$ layers with $x \approx 1$ so as to increase the spectral response of the solar cells at shorter wavelengths, the surface morphology of the higher Al composition AlGaAs layers degraded in a short time. Both $Al_{0.85}Ga_{0.15}As$-GaAs and lattice-matched $Al_{0.85}Ga_{0.15}As$-$GaAs_{1-y}Sb_y$ DH samples were prepared for evaluation.

ORIGINAL PAGE IS
OF POOR QUALITY

Chapter III

LIQUID PHASE EPITAXIAL GROWTH

This chapter first describes melt and substrate preparation. Growth procedures and the quality of the grown samples are then discussed in detail.

A. Growth Technique

The growth conditions have been determined for preparing $Al_xGa_{1-x}As$ and $GaAs_{1-y}Sb_y$ single crystals with specified values of x and y. These values were controlled by adding known amounts of Al or Sb to As-saturated Ga melts. Figure 4 is a diagram of the horizontal sliding-boat LPE growth system (vacuum tight) used in this study and described in detail by Cheung [15]. The samples were grown in flowing H_2 at atmospheric

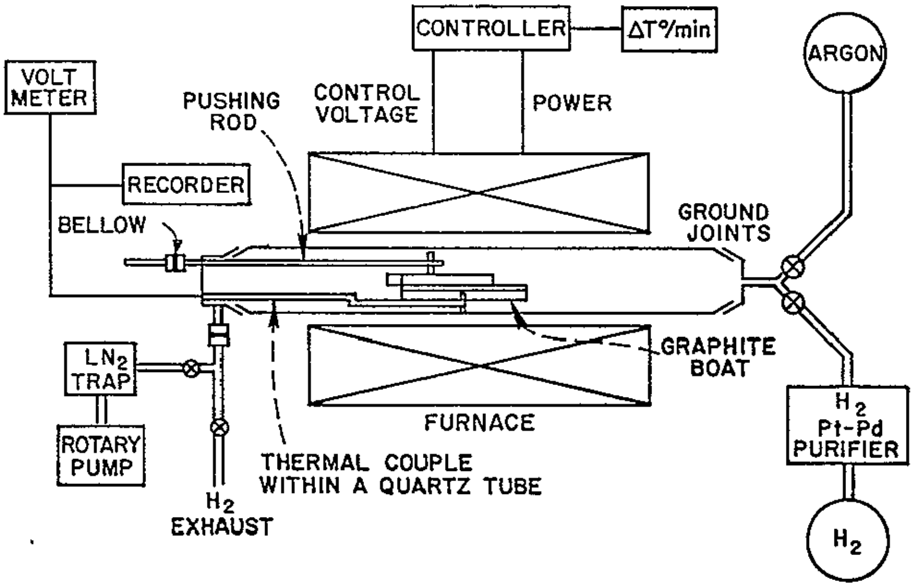

Fig. 4. HORIZONTAL SLIDING BOAT LPE GROWTH SYSTEM.

pressure. The growth temperature was 850° to 820°C, and the cooling rate was 0.2 or 0.4°C/min. All p-type layers were doped with Ge ($p = 2$ to $5 \times 10^{17}/cm^3$ in GaAs and GaAsSb and $\approx 1 \times 10^{18}/cm^3$ in AlGaAs) [16, 17,18]. All n-type layers were doped with Sn ($n \lesssim 10^{17}/cm^3$ in AlGaAs) [16,19].

1. Melt and Substrate Preparation

The GaAs, AlGaAs, and GaAsSb layers were grown by LPE in the Ga-rich corner of the ternary phase diagram. Six 9's pure Ga melts were first baked out in flowing H_2 at 800°C for 12 hours to remove volatile contaminants such as oxygen, and then an undoped polycrystalline GaAs wafer, pure Al, pure Sb, and dopants were added as required.

To ensure melt saturation and to reduce oxide contamination, an undoped GaAs wafer, larger than actually required to saturate the melt at the growth temperature, was placed on the top of each melt. Either Te- or Cr-doped (100) and/or (111)B GaAs substrates (14 mils thick) were loaded in the recess adjoining the melts. The Te-doped GaAs substrate had a carrier concentration of approximately $n = 2 \times 10^{18}/cm^3$.

Before loading into the system, all the materials were successively degreased by trichloroethylene, acetone, and methanol in an ultrasonic bath and then soaked in HCl for three minutes to remove surface oxide. Following this procedure, special care was taken to avoid exposing the materials to air. They were thoroughly rinsed in methanol several times by diluting the HCl solution with methanol and then in hot electronic-grade isopropyl-alcohol and blown dry using filtered N_2 before loading. During preparation, the substrates were held by an especially designed quartz tweezer to avoid surface damage during the cleaning process.

ORIGINAL PAGE IS
OF POOR QUALITY

2. Growth Procedure

Previous growth techniques were modified [15,20] to improve the surface morphology of as-grown multiple layers by reducing the lateral spacing between the GaAs and the AlGaAs melts. This reduction lessens the time when the substrate is exposed to the H_2 flow during transfer from one melt to the next. Growth procedures for p-p-p and p-p-n DH samples will be described using the diagram of the graphite boat in Fig. 5. After loading, the system was purged with H_2, pumped to less than 1 Torr, and then backfilled with H_2 at a flow rate of 120 cc/min.

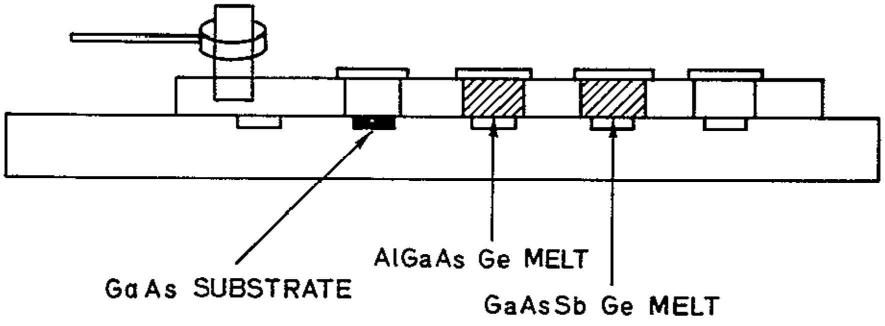

a. p-p-p DH growth system

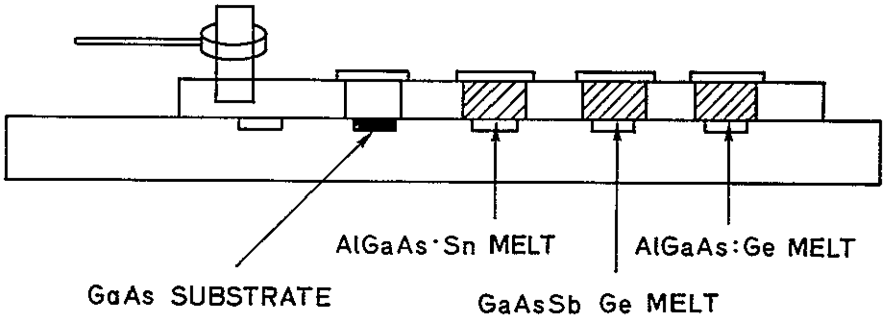

b. p-p-n DH growth system

Fig. 5. SLIDING GRAPHITE-BOAT GROWTH SYSTEM.

In the p-p-p DH growth, AlGaAs and GaAs (or GaAsSb) melts were prepared, and the GaAs substrate was loaded in the recess next to the AlGaAs melt. After the temperature controller was turned on at the initial growth temperature (0.4°C/min cooling rate), the top plate was pulled from the starting position to the left to grow the first AlGaAs layer, pulled to the left a second time to grow the GaAs (or GaAsSb) layer, moved to the right to grow the second AlGaAs, and then was returned to the starting position.

In the p-p-n DH growth, two AlGaAs (one Sn-doped, and the other Ge-doped) and one GaAs (or GaAsSb) melts were prepared. The procedure was similar to the p-p-p DH growth except that the top plate was pulled successively to the left to grow the three layers, after which the furnace was removed and the inlet and outlet valves were closed. When room temperature was reached, the system was returned to its starting position by moving the top plate to the right. The reason for this last procedure is to intentionally grow a thin GaAs layer on the top of the second AlGaAs layer because Al in the grown layer depletes during the cooling process. An ohmic contact to this GaAs layer is easily made.

B. Solidus Composition of Grown Layers

Solidus compositions of the grown AlGaAs and GaAsSb layers were determined by standard electron-microprobe analyses. Both (100)- and (111)B-oriented GaAs substrates were used. Thicknesses of the epitaxial layers were several micrometers, and the accelerating voltage in the electron microprobe was 10 keV.

1. Al Composition

Figure 6 plots the solidus Al composition in $Al_xGa_{1-x}As$ single layers as a function of the weight ratio W_{Al}/W_{Ga} in the melt. For example, crystals with $x = 0.85$ were grown at 840 °C, using an Al/Ga weight ratio of 9.8×10^{-3} in the As saturated melt.

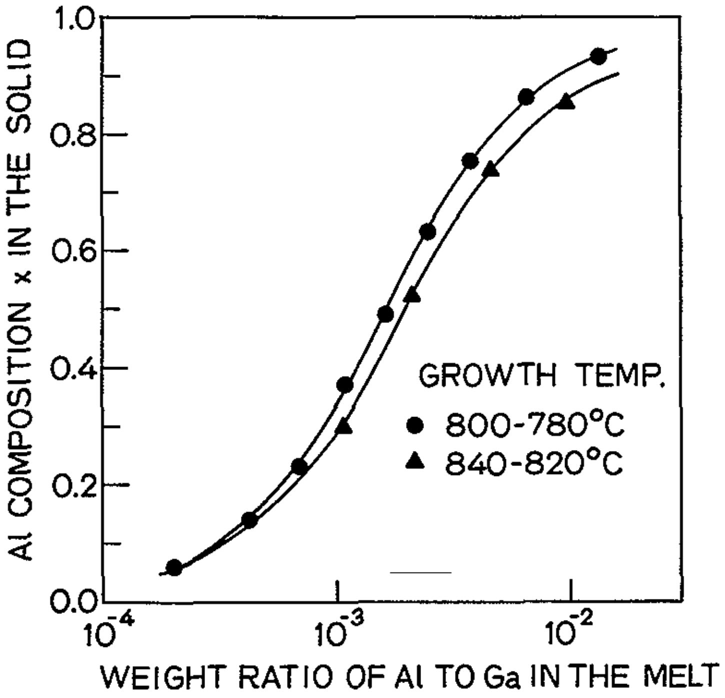

Fig. 6. SOLIDUS Al COMPOSITION IN LPE AlGaAs LAYERS VS WEIGHT RATIO OF Al TO Ga IN THE MELT. Two growth temperature ranges are shown.

Two sets of samples were grown at different temperature ranges. Higher Al compositions were obtained at the lower growth temperature for a given weight ratio because of a higher distribution coefficient of Al at the lower temperature (see Table 1). In addition, the Al distribution coefficient, at a fixed growth temperature, increased when the Al/Ga

Table 1

GROWTH DATA OF LPE AlGaAs SINGLE LAYERS

Sample No.	Melt Weight Ratio W_{Al}/W_{Ga} ($\times 10^{-3}$)	Al Composition x	Al Distribution Coefficient D†
T_G = 840 to 820°C			
201B	1.057	0.299	109.5
201A	2.199	0.520	91.55
152X	4.665	0.738	60.99
140Y	9.731	0.851	33.39
T_G = 800 to 780°C			
113J	0.202	0.06	115.2
114J	0.426	0.14	127.3
115J	0.689	0.23	129.2
116J	1.087	0.37	131.7
117J	1.629	0.49	116.4
118J	2.481	0.63	98.3
119J	3.762	0.75	77.2
120J	6.579	0.86	50.6
121J	13.390	0.93	26.9

†D is the ratio of the atomic fraction of the substituting element in the crystalline solid to that in the liquid melt.

weight ratio in the melt decreased. The same Al composition was obtained on both (100)- and (111)B-oriented GaAs substrates when grown simultaneously from the same melt. This implies that the distribution coefficient of Al is independent of substrate orientation.

2. Sb Composition

Figure 7 plots the solidus Sb composition in $GaAs_{1-y}Sb_y$ single layers as a function of the weight ratio W_{Sb}/W_{Ga} in the melt at a growth

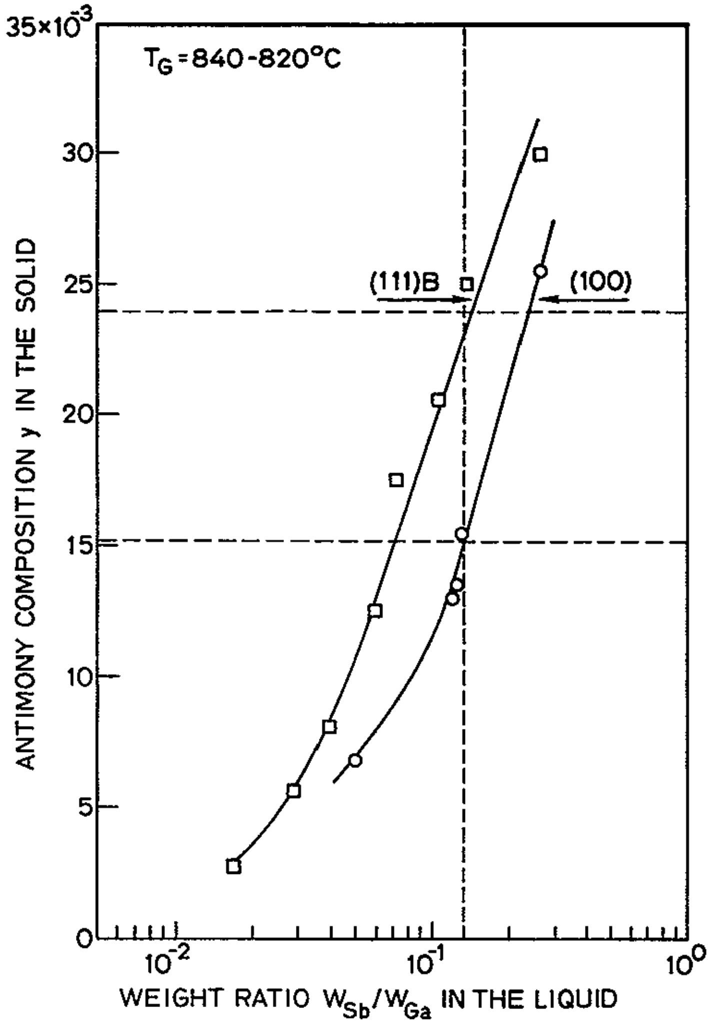

Fig. 7. SOLIDUS Sb COMPOSITION IN LPE $GaAs_{1-y}Sb_y$ LAYERS VS WEIGHT RATIO OF Sb TO Ga IN THE MELT. Results on (100)- and (111)B-oriented GaAs substrates are shown.

temperature of 840 to 820°C. The antimony composition varied from $y = 0$ to $y = 0.03$. Detailed growth information is listed in Table 2. Data points are somewhat scattered because of uncertainty in the Sb compositions. Antimony concentration profiles of very thick (30 μm) GaAsSb single layers, along cleaved edges, indicated that Sb concentration is constant with depth.

Table 2

GROWTH DATA OF LPE GaAsSb SINGLE LAYERS

Sample No.	Melt Weight Ratio W_{Sb}/W_{Ga} $(\times 10^{-2})$	Sb Composition y	Sb Distribution Coefficient D
(100) Orientation			
203	0.0069	0.050	0.241
155X	0.0129	0.120	0.188
153	0.0133	0.125	0.186
206	0.0155	0.130	0.208
154X	0.0251	0.263	0.167
(111)B Orientation			
122Y	0.0027	0.017	0.277
125X	0.0056	0.028	0.349
123Y	0.0082	0.040	0.358
123X	0.0126	0.060	0.367
124X	0.0174	0.074	0.413
124Y	0.0206	0.101	0.356
205	0.0250	0.130	0.336
154Y	0.0300	0.263	0.199

When $GaAs_{1-y}Sb_y$ layers were grown simultaneously on both (100)- and (111)B-oriented GaAs substrates from the same melt, a higher Sb composition y was obtained on the (111)B substrate. For example, at a weight ratio of $W_{Sb}/W_{Ga} = 0.13$, $y = 0.015$ and 0.024 on the (100) and (111)B substrates, respectively. The corresponding Sb distribution coefficients are $D = 0.21$ and 0.34. These observations reveal that Sb has a higher distribution coefficient on the (111)B-oriented substrates (see Table 2).

ORIGINAL PAGE IS
OF POOR QUALITY

It can be seen in Figs. 6 and 7 that $Al_xGa_{1-x}As$-$GaAs_{1-y}Sb_y$ double-heterojunction samples can be grown with a wide range of Al and Sb compositions.

C. Layer Characterization

Figure 8 is a series of photomicrographs of the surface morphology of undoped as-grown single layers (several μm in thickness). The first

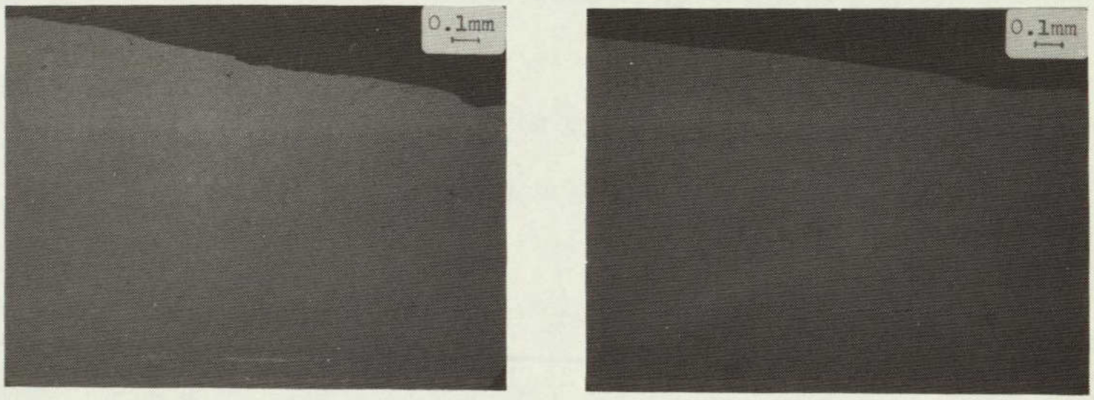

a. $Al_{0.85}Ga_{0.15}As$ b. GaAs

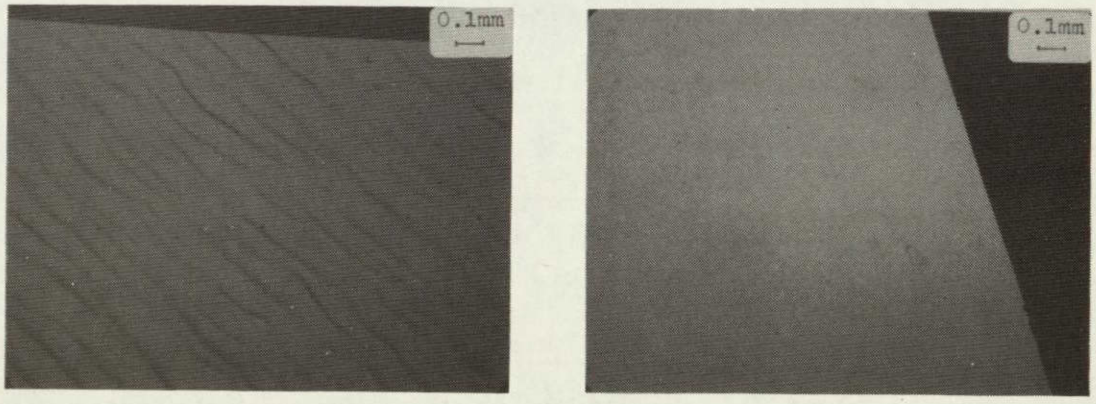

c. $In_{0.01}Ga_{0.99}As$ d. $GaAs_{0.98}Sb_{0.02}$

Fig. 8. PHOTOMICROGRAPHS SHOWING SURFACE MORPHOLOGY OF AS-GROWN LPE SINGLE LAYERS.

two layers (Figs. 8a and 8b) were grown on (100)-oriented GaAs substrates, and the second two layers (Figs. 8c and 8d) were grown on (111)B-oriented GaAs substrates. The surface morphology of the InGaAs layer was very poor, and the layer could be grown on only (111)B-oriented GaAs substrates [21,22,23,24]. The surface morphology of the others was very good.

At the beginning stage of this research, InGaAs layers were grown to provide a zero mismatch with $Al_{0.85}Ga_{0.15}As$. This work was abandoned although the InGaAs layer had better solar-cell spectral response at long wavelengths [4,25] than did the GaAsSb layers when lattice-matched with $Al_{0.85}Ga_{0.15}As$. Poor surface morphology of the InGaAs LPE layers grown in the Ga-rich corner of the ternary phase diagram was the result of inadequate wiping of the melt [26]. The surface morphology of the AlGaAs-InGaAs DH samples was even poorer.

Figure 9 shows the cross section of an $Al_{0.85}Ga_{0.15}As$-GaAs DH sample and its Al line profile as recorded by the electron-microprobe analyzer. The sample was grown on a (100)-oriented GaAs:Te substrate and cleaved with a diamond scriber. The cleaved edge was stained in a PA solution (3 drops NH_4OH + 200 ml H_2O_2: PH = 7) for 10 min and rinsed in methanol [27,28]. It can be observed that all the interfaces are straight and parallel. The layer thicknesses, from left to right, are 5.0, 6.6, and 5.8 μm, respectively.

The electron microprobe had a 10.0 KeV accelerating voltage, and the effective diameter of excitation at this voltage was approximately 6 μm. The line profile, which is a reproduction of the original recording, was used to determine the Al composition x of the $Al_xGa_{1-x}As$ layers by standard microprobe analyses. A value of $x = 0.85 \pm 0.01$ was obtained from the two layers.

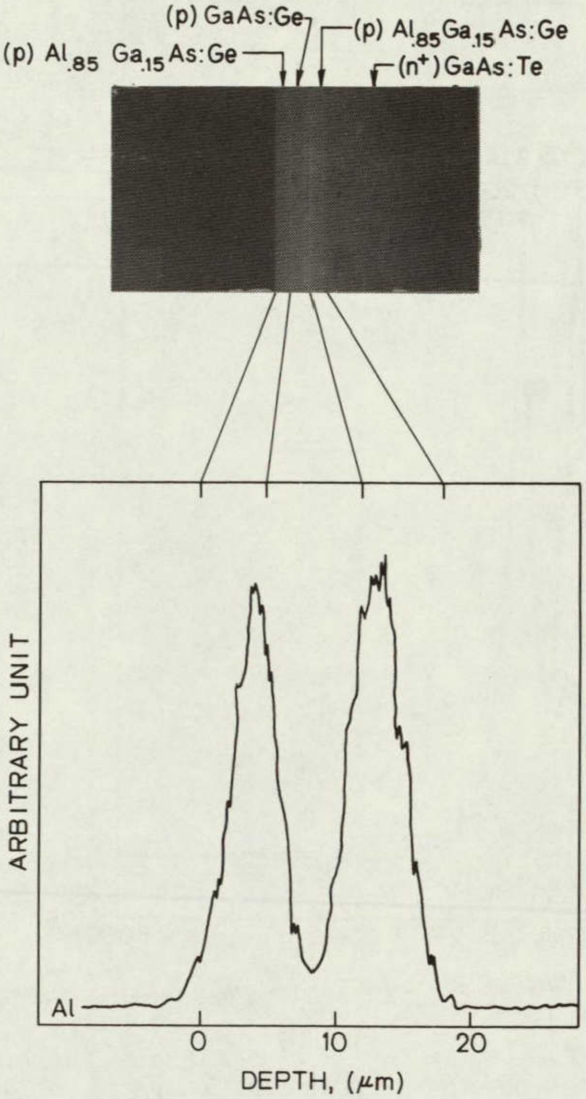

a. Photomicrograph of stained cross section

b. Al concentration profile as obtained from an electron-micrograph recording

Fig. 9. AN $Al_{0.85}Ga_{0.15}As$:Ge-GaAs:Ge DH SAMPLE.

Figure 10 is the PL spectra of the sample in Fig. 9 at room and LN_2 temperatures. A 6471 Å Kr-ion laser was used for excitation. The PL output is from the GaAs:Ge layer only. The band-gap energy of GaAs:Ge shifted from 1.4285 eV at 300 K to 1.5083 eV at 77 K. Although only one peak, caused by band-to-band transitions, was observed at 300 K, two additional peaks are seen at 77 K resulting from transitions from Ge

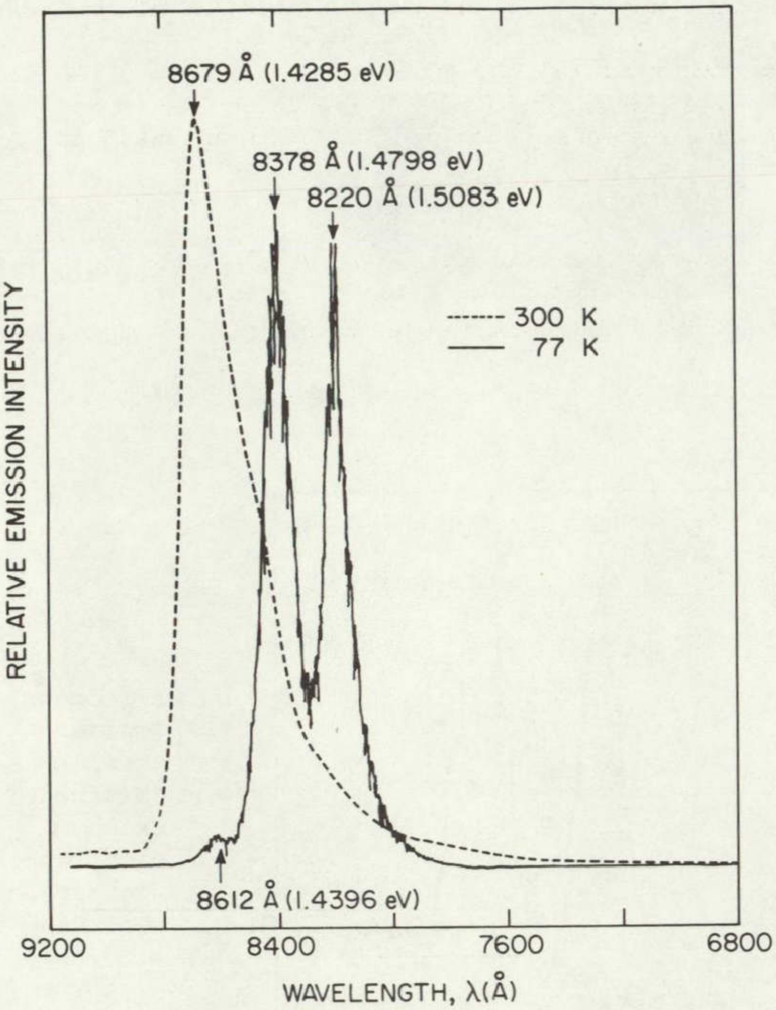

Fig. 10. PHOTOLUMINESCENT SPECTRA OF $Al_{0.85}Ga_{0.15}As$:Ge-GaAs:Ge DH SAMPLE. A 6471 Å Kr laser was used for excitation, and the PL output came from the GaAs:Ge layer only.

impurity levels to the conduction band. The activation energies of these two acceptor levels are 28.5 and 68.7 meV [29,30].

The sharp PL spectrum at 77 K indicates that there was almost no Al concentration gradient at the heterojunction interface. Precise measurements by Auger analysis revealed that the interface-transition width was approximately 210 Å (a nearly abrupt heterojunction) and that there was no detectable cross diffusion of Al (or Sb in the $Al_{0.85}Ga_{0.15}As-GaAs_{1-y}Sb_y$

DH samples) at the interface. Additional details of the Auger measurements have been reported [31,32].

Figure 11 is a cross section of the (100)-oriented $Al_{0.85}Ga_{0.15}As$-$GaAs_{0.985}Sb_{0.015}$ DH diode. Because no energy barrier for majority carriers existed, both p-p and n-n heterojunctions were ohmic. The substrate side of the as-grown sample was lapped to reduce the total thickness to less than 7 mils. The Au + 12%Ge:Ni and Au + 10%Zn alloys were evaporated onto the n-type substrate and the p-type GaAs layer, respectively, and were then alloyed at 450°C for 5 min to form ohmic contacts. After they were cleaved into small pieces (usually less than 2×1 mm^2), each diode was mounted on a TO-5 header.

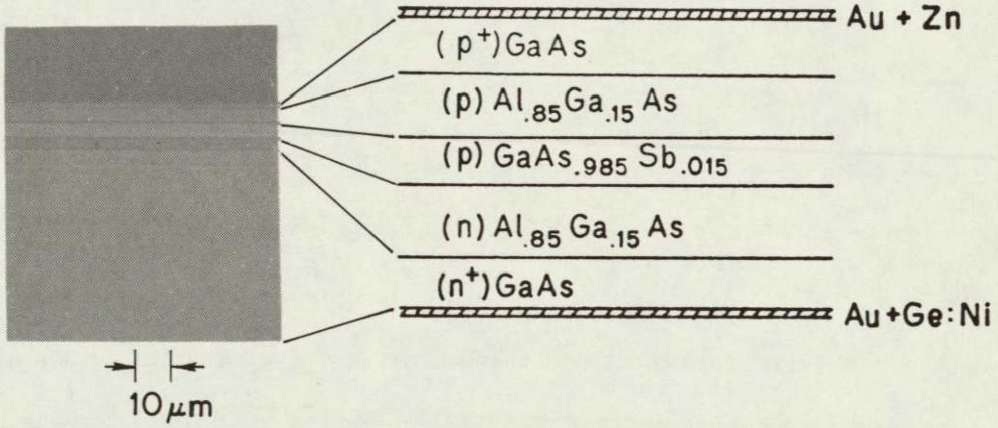

Fig. 11. PHOTOMICROGRAPH OF STAINED CROSS SECTION OF A (100)-ORIENTED $Al_{0.85}Ga_{0.15}As$-$GaAs_{0.985}Sb_{0.015}$ DH DIODE.

Figure 12 shows the I-V characteristic curve and EL output of the above diode at 300 K. In the I-V curve, a threshold voltage of approximately 0.9 V and a breakdown voltage of 5 V were obtained in the forward- and reverse-bias directions, respectively. It was observed that the breakdown voltage of GaAs (or GaAsSb) homojunction diodes was generally

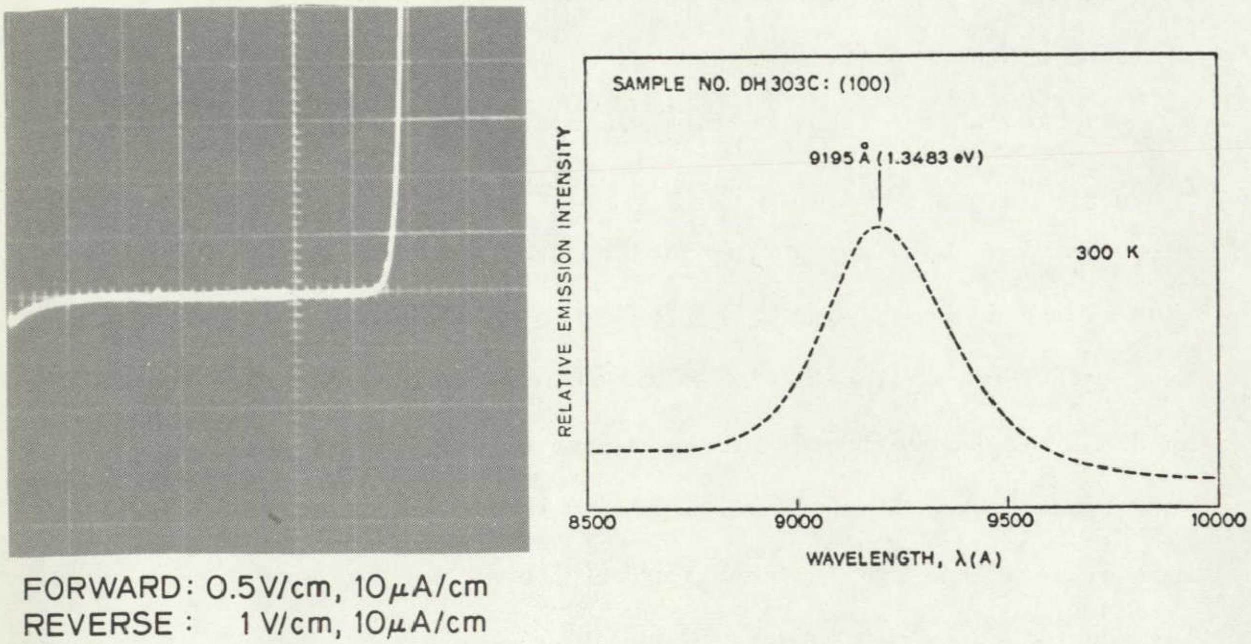

b. EL output

a. I-V characteristic curve

Fig. 12. (100)-ORIENTED $Al_{0.85}Ga_{0.15}As-GaAs_{0.985}Sb_{0.015}$ DH DIODE.

several times higher than that of the DH diodes. The EL output was obtained at a current density of 35 A/cm^2. At the low current-density level, the EL peak (λ = 9195 Å) was located at a longer wavelength than was the PL peak (λ = 8973 Å) for the same amount of Sb ($y = 0.015$). When the current density was increased, the EL peak moved to a shorter wavelength.

Figure 13 shows the arrangement used for measuring minority carrier diffusion length with a scanning electron microscope in the induced-current mode; semi-log plots of induced-current vs beam position are included. For additional details, see Refs. 20, 33, and 34. A (100)-oriented $Al_{0.85}Ga_{0.15}As-GaAs_{0.985}Sb_{0.015}$ DH diode (see inset) was used to measure the diffusion lengths in both the (p)GaAsSb and (n)AlGaAs layers. The corresponding carrier concentrations were (2 to 5) $\times 10^{17}/cm^3$ and $\lesssim 10^{17}/cm^3$, respectively. The electron beam energy for the measurements was 25 keV.

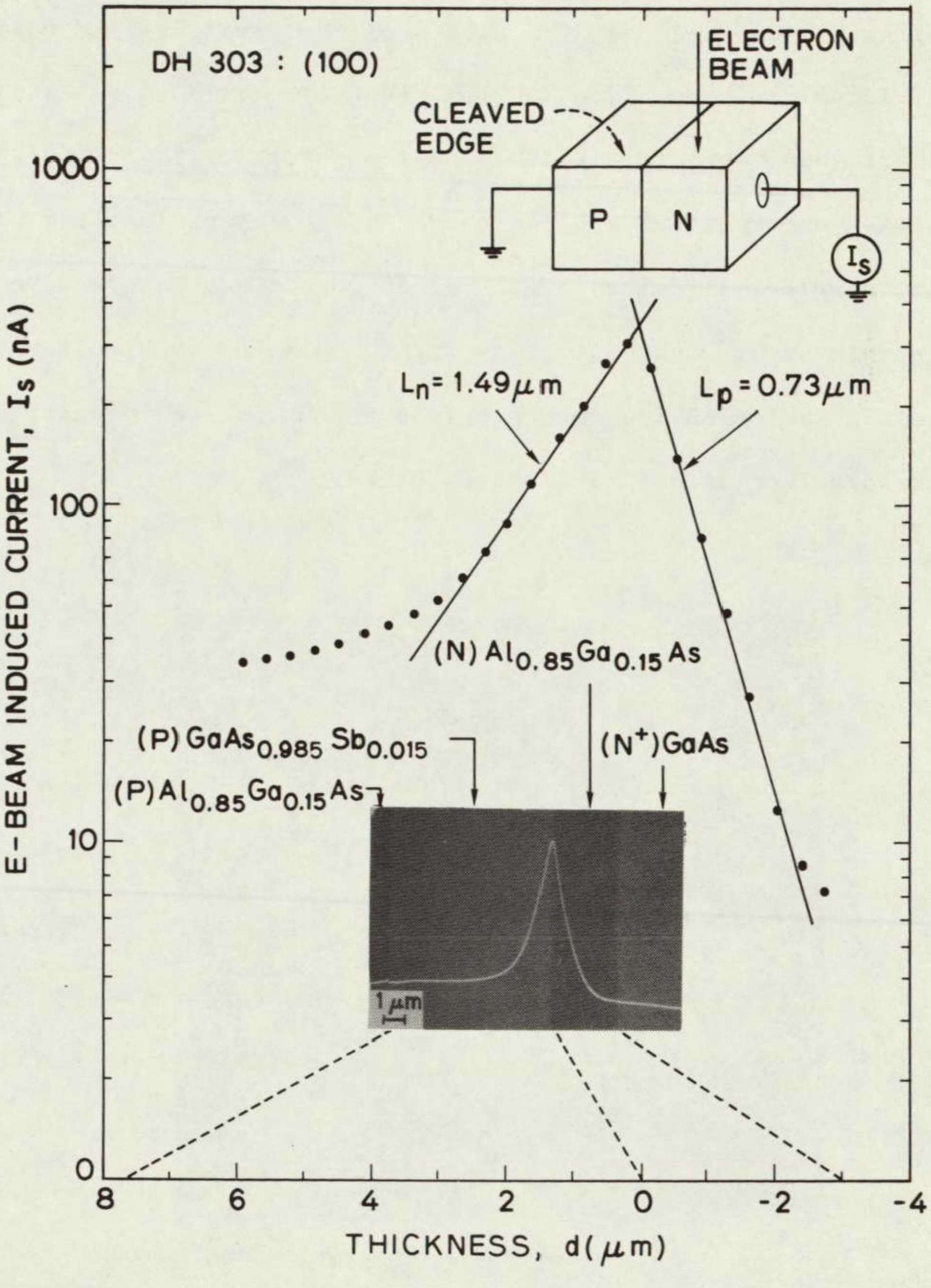

Fig. 13. SCANNING ELECTRON MICROSCOPE INDUCED-CURRENT MODE AND SEMI-LOG PLOTS OF INDUCED-CURRENT VS BEAM POSITION.

The inset at the bottom of Fig. 13 is an induced-current trace superimposed on the secondary emission image, and the position of the p-n junction is identified from the peak of this trace. The minority carrier diffusion lengths obtained from the slopes of the straight-line regions in the semi-log plots were $L_n = 1.49\ \mu m$ and $L_p = 0.73\ \mu m$. The exceptionally short length of L_n [24] may be the result of the cross-hatched patterns always observed on (100)-oriented GaAsSb layers (see Fig. 14). The minority carrier diffusion lengths of Ge-doped GaAs layers were not measured in this study; instead, $L_n = 12\ \mu m$ obtained by Ettenberg et al [6] was used in the evaluation of interface recombination velocity at an AlGaAs-GaAs interface as described in Chapter V.

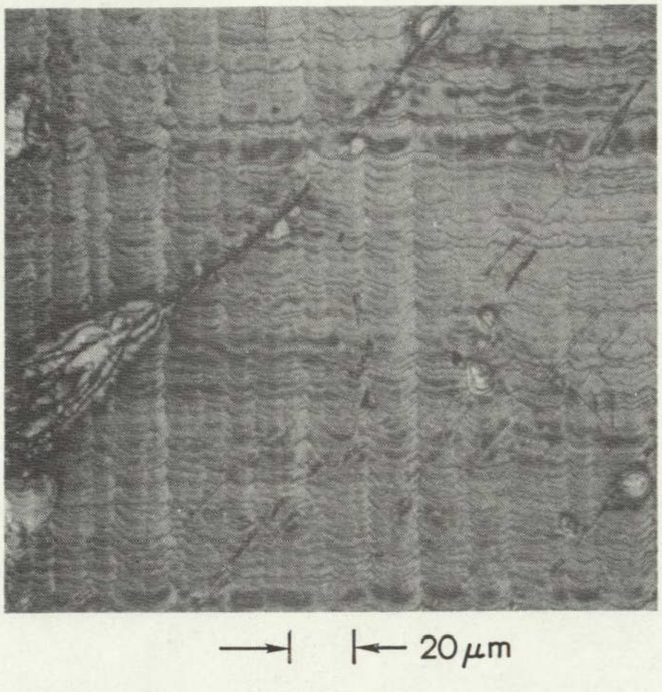

Fig. 14. PHOTOMICROGRAPH OF SURFACE MORPHOLOGY OF AS-GROWN (100)-ORIENTED $Al_{0.85}Ga_{0.15}As-GaAs_{0.985}Sb_{0.015}$ DH DIODE.

Chapter IV

STRAINED AND STRAIN-FREE LATTICE MISMATCH

When heteroepitaxial layers are grown, two types of defects [35,36,37] can usually be observed because of differences in the lattice constants and thermal expansion coefficients (see Fig. 15). In this chapter, the resulting bending [38] of the wafer and lattice defects introduced during growth (stacking faults) [35] are neglected. Attention is focused only on methods for obtaining the relative lattice mismatch between the heteroepitaxial layer and the substrate.

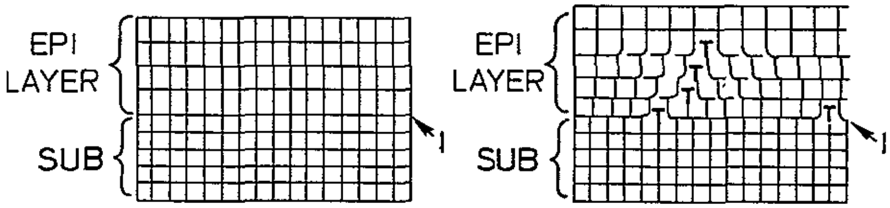

a. Elastic lattice deformation

b. Misfit dislocations

Fig. 15. DEFECTS AT HETEROJUNCTION INTERFACES. "I" indicates the epitaxial layer-substrate interface.

If there are no misfit dislocations at the heterojunction interface, the lattice mismatch is relieved by elastic lattice deformation of the epitaxial layer, caused by stress at the interface, in which the spacing of the lattice planes normal to the growth surface does not change, but the spacing of the lattice planes parallel to the growth surface expands or contracts. In other words, the lattice constant of the epitaxial layer becomes uniform along the growth direction and much of the elastic strain resulting from the lattice mismatch remains in the layer. It has been reported [36,37,39,40,41] that, in cubic and zincblende III-V compounds, the lattice of the epitaxial layer can be "tetragonally" deformed on (100) substrate orientations but "rhombohedrally" deformed on (111) substrate orientations.

When the lattice mismatch cannot be relieved by elastic lattice deformation, however, a misfit dislocation array (unidirectional or cross hatched) [35] is produced and most of the strain is relieved in the vicinity of the interface. The epitaxial layer is closer to perfect crystalline structure when misfit dislocations are present. Recent studies [35,42] demonstrated that layer-strain energy and the generation of interfacial misfit dislocations at the growth temperature are functions of lattice misfit and layer thickness. Thick layers or a large misfit cause cross-hatched dislocations.

In both defects illustrated in Fig. 15, the relative lattice mismatch between the epitaxial layer and substrate can be obtained directly from measurements of the separation angles between the $K_{\alpha 1}$ peaks in X-ray diffraction profiles (so-called "rocking curves"). A method is derived below, based on the generalized diagram in Fig. 16, to obtain lattice mismatch and lattice constants.

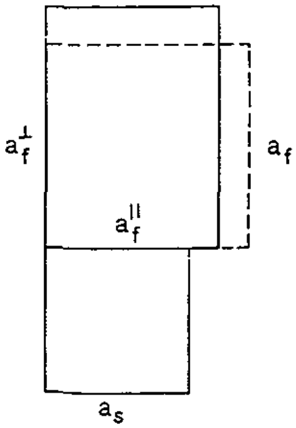

Fig. 16. DEFORMED AND UNDEFORMED LATTICES OF AN EPITAXIAL LAYER ON AN UNDEFORMED SUBSTRATE.

In Fig. 16, a_s is the lattice constant of the substrate, $a_f^{\perp}$ and $a_f^{\parallel}$ are the strained lattice constants of the epitaxial layer perpendicular and parallel to the substrate surface, and a_f is the lattice constant of the epitaxial layer in the stress-free state. For convenience, these parameters are defined as $\Delta a^{\perp} = a_f^{\perp} - a_s$, $\Delta a^{\parallel} = a_f^{\parallel} - a_s$, and $\Delta a = a_f - a_s$. It has been observed [37,39,40] that, in elastic lattice deformation,

$$\frac{\Delta a^{\perp}}{a_s} \gg \frac{\Delta a^{\parallel}}{a_s} \approx 0 \tag{4.1}$$

If $\Delta\theta_1$ is the separation angle between the $K_{\alpha 1}$ peaks of the substrate and epitaxial layer and if $\Delta\theta_2$ is the same quantity measured after rotating the crystal by 180° around the normal to the substrate surface, the angular difference caused by the variation in lattice spacing $\Delta\theta_B$ is

$$\Delta\theta_B = \frac{\Delta\theta_1 + \Delta\theta_2}{2} \tag{4.2}$$

In this measurement, $\Delta\theta_1 \neq \Delta\theta_2$ principally because of misorientation of the substrate itself.

The difference in lattice spacing $\Delta a^{\perp}$ was determined through the following equation which was obtained by differentiating Bragg's law:

$$\frac{\Delta a^{\perp}}{a_s} = -\cot\,\theta_B \times \Delta\theta_B \tag{4.3}$$

where θ_B is the Bragg angle.

From the stress-strain relationship of a cubic crystal, the following equations (see the Appendix for their derivation) are obtained by assuming $\sigma_{xx} = \sigma_{yy} = \sigma^{\parallel}$ and $\sigma_{zz} = \sigma^{\perp} = 0$:

$$\sigma^{\parallel} = \epsilon^{\parallel} \frac{E}{1 - \nu_{eff}} \tag{4.4}$$

and

$$\epsilon^{\perp} = \epsilon^{\parallel} \frac{-2\nu_{eff}}{1 - \nu_{eff}} \tag{4.5}$$

where σ is the stress and ϵ is the strain, and E and ν_{eff} are Young's modulus and the effective Poisson ratio, respectively. The elastic constants of the layer and the substrate are assumed to be equal [38]. The strains $\epsilon^{\parallel}$ and $\epsilon^{\perp}$ are expressed in terms of $\Delta a^{\perp}/a_s$, $\Delta a^{\parallel}/a_s$, and $\Delta a/a_s$ by

$$\epsilon^{\perp} = \frac{a_f^{\perp} - a_f}{a_f} = \frac{\Delta a^{\perp} - \Delta a}{a_f} \approx \frac{\Delta a^{\perp}}{a_s} - \frac{\Delta a}{a_s} \tag{4.6}$$

and

$$\epsilon^{\parallel} = \frac{a_f^{\parallel} - a_f}{a_f} = \frac{\Delta a^{\parallel} - \Delta a}{a_f} \approx \frac{\Delta a^{\parallel}}{a_s} - \frac{\Delta a}{a_s} \tag{4.7}$$

From the Eqs. (4.1), (4.5), (4.6), and (4.7),

$$\epsilon^{\perp} = \frac{2\nu_{eff}}{1 + \nu_{eff}} \frac{\Delta a^{\perp}}{a_s} = \frac{2\nu_{eff}}{1 - \nu_{eff}} \frac{\Delta a}{a_s} \tag{4.8}$$

The strain-free relative lattice mismatch can be expressed from the above as

$$\frac{\Delta a}{a_s} = \frac{1 - \nu_{eff}}{1 + \nu_{eff}} \frac{\Delta a^{\perp}}{a_s} \tag{4.9}$$

The strained and strain-free lattice mismatches have been obtained from Eqs. (4.3) and (4.9), respectively. For misfit dislocations, $(\Delta a/a_s) = -\cot \theta_B \times \Delta\theta_B$ and no effective Poisson ratio is involved.

A. Experiment

The separation angles between the $K_{\alpha 1}$ peaks were precisely measured by an X-ray double-crystal diffractometer. The X-ray target was Cu, and the first crystal was dislocation-free (100) Si. To provide a highly parallel incident beam to the specimen, $CuK_{\alpha2}$ radiation was cut off with an appropriate slit after the (400) reflection of the first crystal, and $\lambda(CuK_{\alpha1}) = 1.54051$ Å. The X-ray penetration depth was estimated to be smaller than 20 μm.

Both (100)- and (111)B-oriented GaAs substrates were used to grow epitaxial layers, and measurements were made at room temperature on the (400) and (444) planes, respectively, for the best precision. The Bragg angles were 33.02° and 70.72° for the (400) and (444) reflections of GaAs ($a_o = 5.6532$ Å). The thicknesses of the substrates were approximately 350 μm, and the thicknesses of the epitaxial layers were 1 to 4 μm.

1. AlGaAs-GaAs Interface

Addition of Al to the GaAs melt increases the lattice constant of the AlGaAs crystals as compared to GaAs. LPE $Al_xGa_{1-x}As$ single layers were grown at 840° to 820°C on both (100)- and (111)B-oriented GaAs substrates as the amount of Al in the melt was changed (see Chapter III).

The Al composition x was independently evaluated by an electron-microprobe analyzer. As discussed in Chapter III, the desired values of x were obtained by changing the weight ratio of Al to Ga in the melt (no normalization was used). Figure 17 presents typical X-ray diffraction profiles, and the resulting data are summarized in Table 3. Although the theoretical value of the full width at half maximum (FWHM) of the rocking curve for a perfectly flat sample is 8.5 seconds, approximately 23 and 143 seconds were observed for (400) and (444) reflections, respectively.

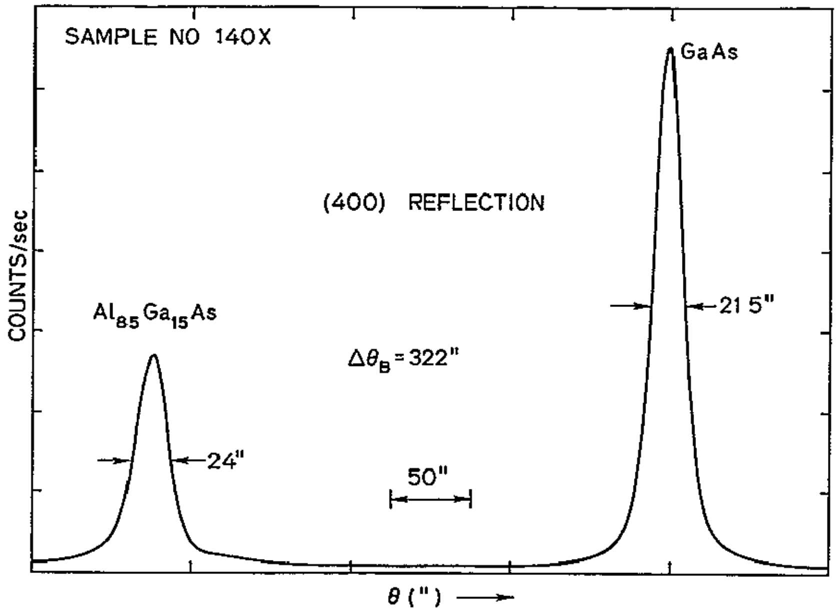

a. (100)-oriented substrate

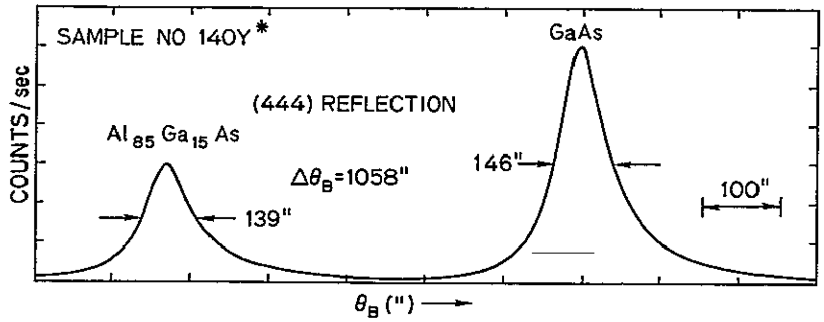

b. (111)B-oriented substrate

Fig. 17. X-RAY DIFFRACTION PROFILES OF LPE $Al_{0.85}Ga_{0.15}As$ LAYERS GROWN ON (100)- AND (111)B-ORIENTED GaAs SUBSTRATES.

Figures 18 and 19 plot the measured strained lattice mismatch and the corresponding individual lattice constant as a function of Al composition. The results are consistent with the linear behavior predicted by Vegard's law. The best fit for (100)-oriented $Al_xGa_{1-x}As$ epitaxial layers was obtained as $(\Delta a^{\perp}/a_s)(Al_xGa_{1-x}As) = (3.54 \times 10^{-5}) + (28.06 \times 10^{-4})x$.

Table 3

EXPERIMENTAL DATA OBTAINED FROM LATTICE-CONSTANT MEASUREMENTS OF AlGaAs SINGLE LAYERS

Sample No.	Al Composition x	$\Delta a^{\perp}/a_s$ ($\times 10^4$)	a_o (Å)
HP1	0.130	3.953	5.6544
HP2	0.213	6.415	5.6551
HP3	0.249	7.310	5.6554
HP4	0.282	8.354	5.6557
HP5	0.308	9.398	5.6560
HP6	0.384	11.114	5.6565
117J	0.489	14.023	5.6574
118J	0.627	17.603	5.6584
119J	0.751	20.512	5.6593
09	0.783	21.556	5.6596
140X	0.851	24.018	5.6603
206	0.846	24.34	5.6604
73	0.899	25.24	5.6607
50	0.939	25.84	5.6609
201B†	0.299	7.375	5.6560
201A†	0.520	12.110	5.6579
152X†	0.738	15.941	5.6595
140Y†	0.851	17.943	5.6603

†These samples are grown on (111)B GaAs substrates; all others are on (100) GaAs substrates.

Although $\nu_{eff} = 0.312$ [42] was adopted for the (100) GaAs substrate orientation to determine the strain-free lattice mismatch, $\nu_{eff} = 0.190$ was estimated for the (111)B substrate orientation from the ratio of strained lattice mismatch between (100) and (111)B orientations (see Fig. 18). Although one theoretical estimate [42] indicated $\nu = 0.303$ for (111) GaAs orientation, no other experimental data are available.

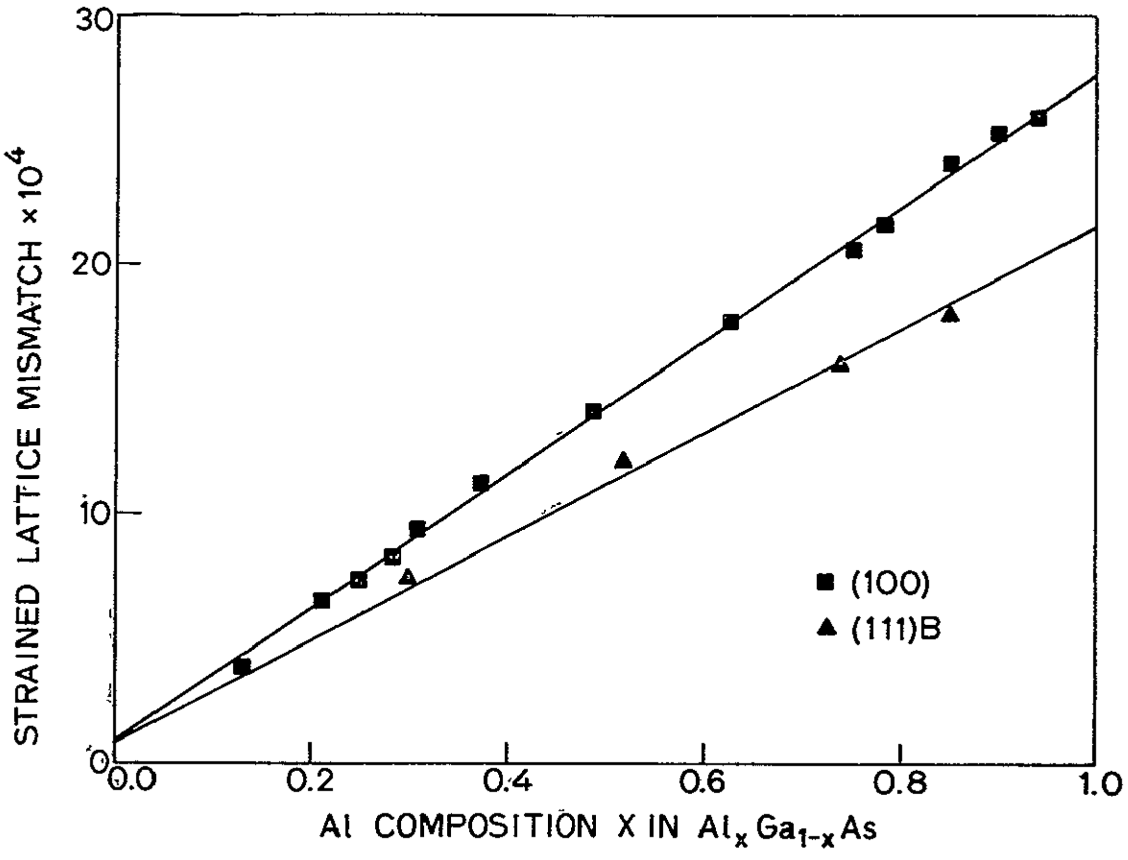

Fig. 18. STRAINED LATTICE MISMATCH BETWEEN THE $Al_xGa_{1-x}As$ EPITAXIAL LAYER AND THE GaAs SUBSTRATE AT 300 K AS A FUNCTION OF Al COMPOSITION x.

To attain individual lattice constants from the strain-free lattice mismatch (Fig. 19), a_o(GaAs) = 5.6532 Å was assumed. It should be emphasized that, for multiple-layer structures, a double-crystal diffractometer yields only precise lattice mismatch. In the best-fit curve in Fig. 19, $a_o(Al_xGa_{1-x}As) = 5.6532 + 0.0084x$ Å which is in good agreement with the result obtained by Estop et al [38].

It should be noted that $Al_xGa_{1-x}As-Al_{x'}Ga_{1-x'}As$ $(x > x')$ double-layer samples have the same separation angles as those in single layers grown from the same melts. In other words, there is no shift in the separation angle caused by the interaction between the epitaxial layer and the substrate.

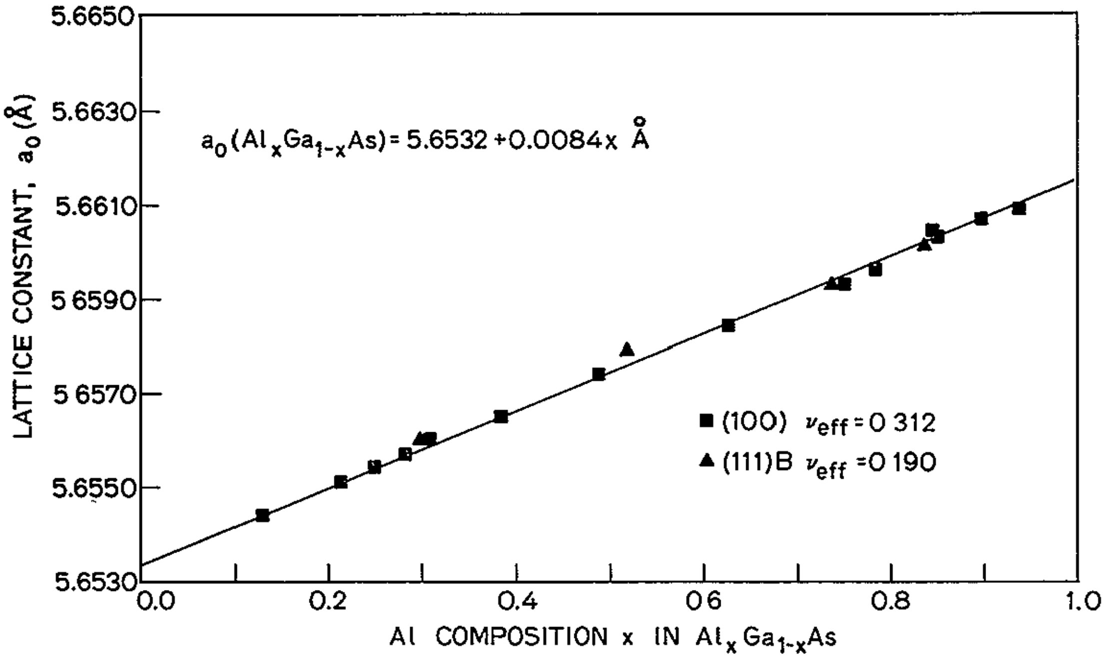

Fig. 19. STRAIN-FREE LATTICE CONSTANT OF $Al_xGa_{1-x}As$ SINGLE LAYERS ON DIFFERENT SUBSTRATE ORIENTATIONS AS A FUNCTION OF Al COMPOSITION x. T = 300 K.

In conclusion, AlGaAs epitaxial layers showed only elastic lattice deformation regardless of GaAs substrate orientation. The reason for this is that there is almost a zero-lattice mismatch between the AlGaAs layer and the GaAs substrate at the growth temperature (see Fig. 22).

2. GaAsSb-GaAs Interface

Just as in the $Al_xGa_{1-x}As$ ternary compound, the addition of Sb to GaAs causes an increase in the lattice constant. LPE $GaAs_{1-y}Sb_y$ single layers were grown at 840° to 820°C on both (100) and (111)B GaAs substrates by changing the amount of Sb in the melt (see Chapter III). Although the surface morphology of layers grown on (111)B substrates appeared smooth, the surfaces of most (100) samples displayed cross-hatched patterns as the result of misfit dislocations at the interface.

Assuming that the cross-hatched pattern indicates no elastic lattice deformation, ν_{eff} was set equal to 0 for a (100)-oriented layer; in other words, strain-free lattice mismatch can be obtained directly from the separation angles of the X-ray diffraction profiles. In (111)B-oriented GaAs substrates, the same effective Poisson ratio $(\nu_{eff} = 0.190)$ as in AlGaAs layers was used, assuming that the elastic constants of the layer and the substrate are equal [38]. The data resulting from these measurements and analyses are summarized in Table 4. As observed in Chapter III, the data points are somewhat scattered because of uncertainty in the Sb compositions.

Figure 20 plots the strain-free lattice constants of GaAsSb single layers grown on (100) and (111)B GaAs substrates as a function of Sb composition. Two interesting results are observed. The first is that, when $a_o(\text{GaSb}) = 6.0959$ Å, both (100) and (111)B GaAsSb layers deviate slightly from Vegard's law. The other is that lattice-matched $Al_{0.85}Ga_{0.15}As-GaAs_{1-y}Sb_y$ double layers can be grown at different Sb compositions, depending on substrate orientation; namely, (100) $Al_{0.85}Ga_{0.15}As-GaAs_{0.985}Sb_{0.015}$ and (111)B $Al_{0.85}Ga_{0.15}As-GaAs_{0.976}Sb_{0.024}$ double-heterojunction samples with zero lattice mismatch were grown from melts with a weight ratio of $W_{Sb}/W_{Ga} = 0.13$ and a growth temperature of $T_G = 840$ to 820°C. These samples were used in evaluating the measurements of interface recombination velocity as described in Chapter V. Figure 21 is the X-ray diffraction profile of a lattice-matched $Al_{0.85}Ga_{0.15}As-GaAs_{0.976}Sb_{0.024}$ double layer grown on a (111)B GaAs substrate. The AlGaAs and GaAsSb $K_{\alpha 1}$ peaks cannot be resolved because of the extremely close lattice match.

Table 4

EXPERIMENTAL DATA OBTAINED FROM LATTICE-CONSTANT MEASUREMENTS OF GaAsSb SINGLE LAYERS

Sample No.	Sb Composition y	$\Delta a^{\perp}/a_s$ ($\times 10^4$)	$\Delta a/a_s$ ($\times 10^4$)	a_o (Å)
203	0.0069	----	6.04	5.6566
155X	0.0129	----	11.97	5.6600
153	0.0133	----	12.18	5.6601
206	0.0155	----	13.27	5.6607
154X	0.0251	----	22.26	5.6658
122Y†	0.0027	2.33	1.58	5.6541
125X†	0.0056	4.16	2.83	5.6548
123Y†	0.0064	6.15	4.18	5.6556
203†	0.010	8.44	5.74	5.6564
123†	0.0098	8.90	6.05	5.6566
129†	0.0098	11.15	7.58	5.6575
155Y†	0.0181	13.94	9.48	5.6586
161L†	0.0218	16.45	11.19	5.6595
124Y†	0.0166	15.08	10.25	5.6590
202B†	0.0249	19.84	13.49	5.6608
205†	0.0250	18.76	12.76	5.6604
154Y†	0.030	34.02	23.13	5.6663

†These samples are grown on (111)B GaAs substrates; all others are on (100) GaAs substrates.

In the above analysis of GaAsSb layers, elastic lattice deformation or misfit dislocations were assumed. In reality, both conditions may occur simultaneously [43], which would produce another uncertainty in addition to the microprobe analysis errors.

Although misfit dislocations in (100) $GaAs_{1-y}Sb_y$ layers are assumed, the results from the double layers (see Table 5) reveal that

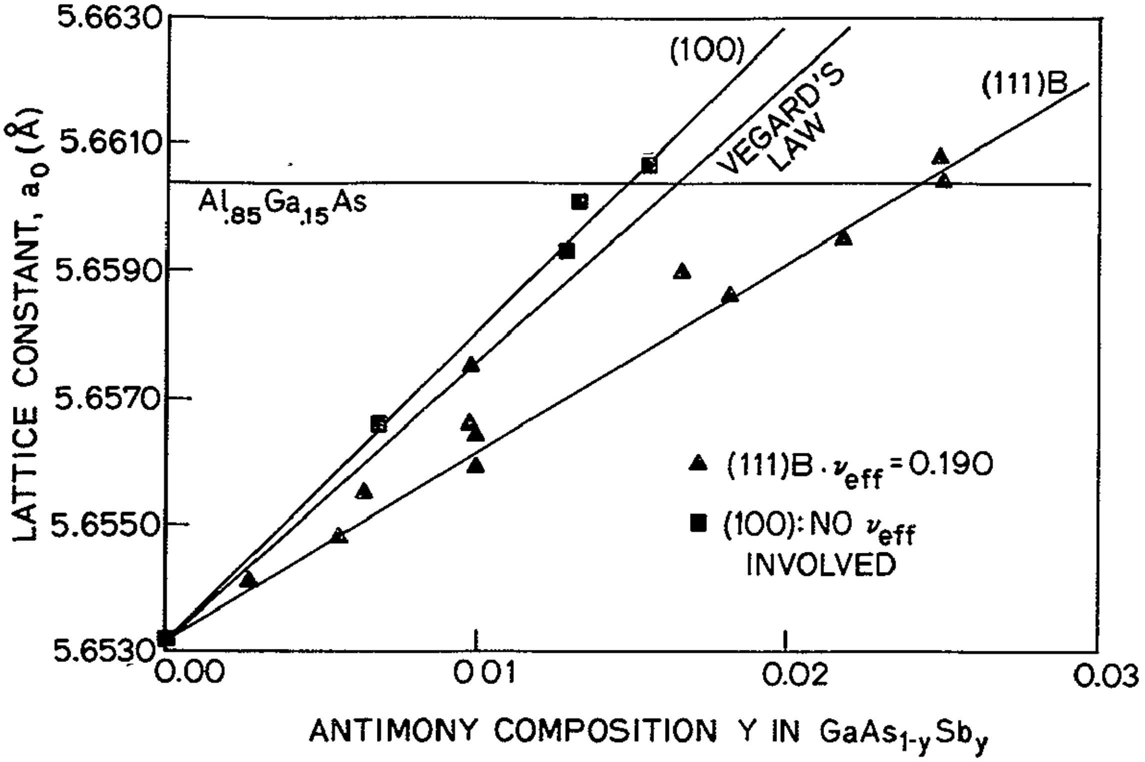

Fig. 20. STRAIN-FREE LATTICE CONSTANTS OF $GaAs_{1-y}Sb_y$ SINGLE LAYERS ON DIFFERENT SUBSTRATE ORIENTATIONS AS A FUNCTION OF Sb COMPOSITION. T = 300 K.

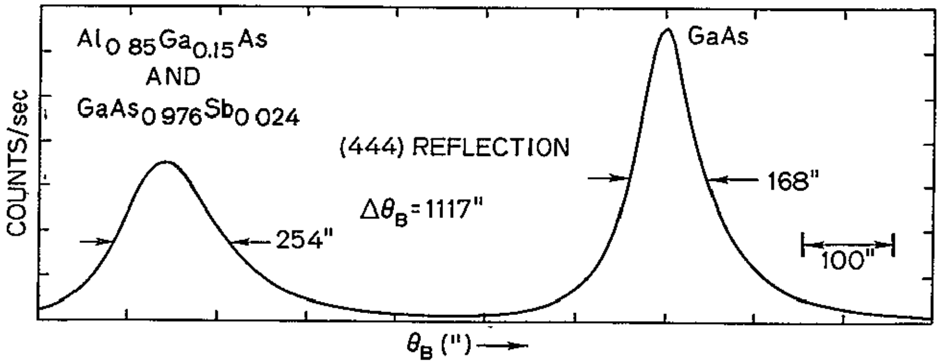

Fig. 21. X-RAY DIFFRACTION PROFILE OF $Al_{0.85}Ga_{0.15}As$-$GaAs_{0.976}Sb_{0.024}$ DOUBLE LAYER GROWN ON (111)B GaAs SUBSTRATE. T = 300 K.

ORIGINAL PAGE IS
OF POOR QUALITY

Table 5

EXPERIMENTAL DATA OF LATTICE CONSTANT MEASUREMENTS OF $Al_{0.85}Ga_{0.15}As$-$GaAs_{1-y}Sb_y$ DOUBLE LAYERS

Sample No.		Sb Composition y	$\Delta a^{\perp}/a_s$ ($\times 10^4$)	$\Delta a/a_s$ ($\times 10^4$)	a_o (Å)
D203	AlGaAs GaAsSb	0.0069	23.27	12.20 5.90	5.6601 5.6565
D203†	AlGaAs GaAsSb	0.010	17.86 7.12	12.15 4.84	5.6601 5.6559
D204	AlGaAs GaAsSb	0.0155	22.02‡	11.55	5.6597
D206†	AlGaAs GaAsSb	0.025	17.64‡	12.00	5.6600
D155Z†	AlGaAs GaAsSb	0.0218	18.94‡	13.30	5.6607

†Elastic lattice deformation and misfit dislocations were assumed in the AlGaAs and GaAsSb layers, respectively.

‡These separation angles are not resolvable.

they could be either elastic lattice deformation (sample D204) or misfit dislocations (sample D203). In addition, lattice constants obtained from the double layers are slightly different than those from single layers, which may be the result, in part, of the uncertainty in ν_{eff}.

B. Discussion

During the analysis of the data, the effects of instrumental broadening (divergence of the beam, focal-spot size, slit width, and spectral width of the X-ray emission wavelength), dislocations and mechanical surface damage on the X-ray diffraction profile were not taken into account.

Actually, FWHM increases with increasing curvature and dislocations. Although absolute values of the lattice constants could not be obtained, the precise separation angle between the two $K_{\alpha 1}$ peaks could be measured. The error in the separation angle caused by the thicknesses of the epitaxial layers was negligible.

The above X-ray measurements in Tables 3 and 4 were made on undoped AlGaAs and GaAsSb single layers. As a result, there may be an additional lattice mismatch on the actual devices caused by the doping of epitaxial layers [36]. Recently, Schiller [41] observed that AlGaAs layers grown on (111)A-oriented GaAs substrates had slightly lower lattice constants than those on (100) because he assumed the same elastic constants $(E/1-\nu)$ for both (100) and (111)A orientations.

Figure 22 plots variations of the lattice constants of GaAs, $Al_{0.85}Ga_{0.15}As$, and $GaAs_{0.985}Sb_{0.015}$ over a 0 to 1000°C temperature range where the thermal expansion coefficient α of the ternary compounds is assumed to follow a linear relationship between those of the two end binary compounds. As has been discussed, AlGaAs epitaxial layers showed elastic lattice deformation only because the lattice mismatch between the AlGaAs layer and GaAs substrate became almost zero at the growth temperature. The $Al_{0.85}Ga_{0.15}As$-$GaAs_{0.985}Sb_{0.015}$ layers, however, showed large lattice mismatch at the growth temperature although the mismatch became zero at room temperature. The large lattice mismatch between $GaAs_{0.985}Sb_{0.015}$ and GaAs at the growth temperature can explain the cross-hatched pattern observed on (100) GaAsSb epitaxial layers. No explanation can be made why elastic lattice deformation was observed on (111)B GaAsSb epitaxial layers. Although the lattice mismatch between the AlGaAs and GaAsSb epitaxial layers is zero, even the lattice-matched samples display strong

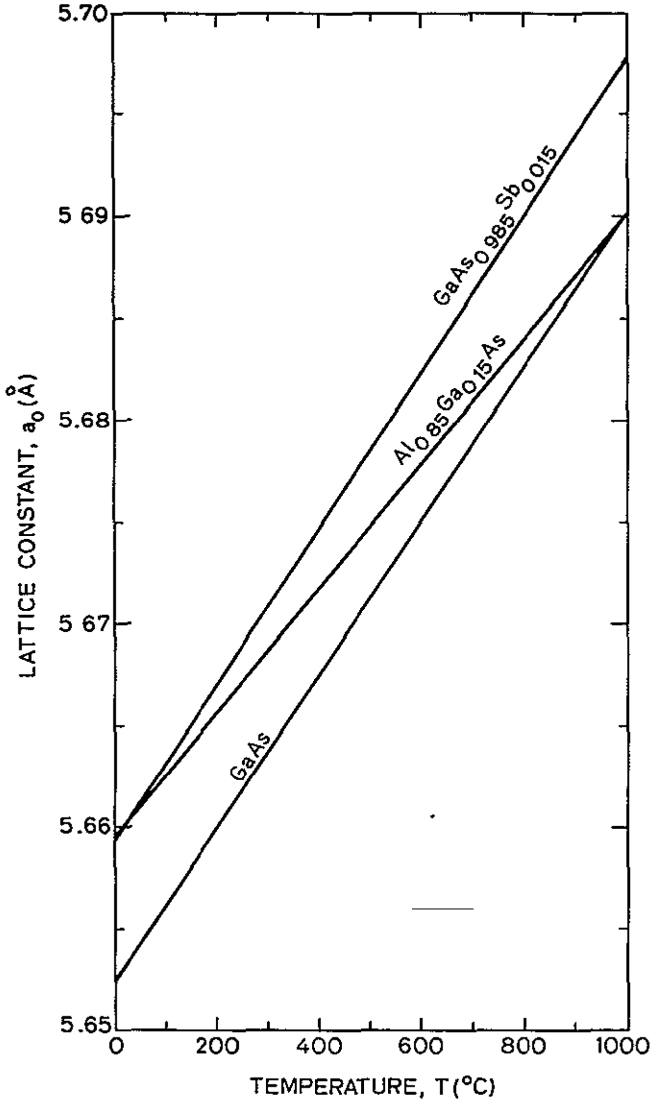

Fig. 22. VARIATION OF LATTICE CONSTANTS OF GaAs, $Al_{0.85}Ga_{0.15}As$ AND $GaAs_{0.985}Sb_{0.015}$ OVER THE TEMPERATURE RANGE OF 0 TO 1000°C. It was assumed that a_0(GaAs) = 5.6532 Å, a_0(AlAs) = 5.6622 Å, and a_0(GaSb) = 6.0959 Å at 300 K. It was also assumed that α(GaAs) = 6.63×10^{-6}/°C [44], α(AlAs) = 5.20×10^{-6}/°C [45], and α(GaSb) = 6.70×10^{-6}/°C [46] over the entire temperature range.

strain [35] between the first epitaxial layer and the substrate because of lattice mismatch. Poorer device performance than expected from perfectly lattice-matched samples, therefore, may be observed.

In conclusion, lattice-matched AlGaAs-GaAsSb layers can be grown on both (100) and (111)B GaAs substrates from the information in Figs. 19 and 20. For example, (100) $Al_{0.85}Ga_{0.15}As$-$GaAs_{0.985}Sb_{0.015}$ and (111)B $Al_{0.85}Ga_{0.15}As$-$GaAs_{0.976}Sb_{0.024}$ double-heterojunction samples with zero lattice mismatch were grown for evaluation from melts with a weight ratio of $W_{Sb}/W_{Ga} = 0.13$ and a growth temperature of $T_G = 840$-$820\,^\circ C$.

Chapter V

EFFECTIVE LIFETIME MEASUREMENT

This chapter describes EL time-decay and optical phase-shift techniques for obtaining effective lifetime and phase-shift measurements, respectively. Interface recombination velocities are determined by curve fitting and are discussed in detail as a function of lattice mismatch.

A. EL Time-Decay

Figure 23 is a diagram [6] of the equipment employed to obtain effective lifetime measurements on p-p-n DH diodes. The preparation, I-V characteristics, and EL output of the samples were described in Chapter III.

The diodes were excited by 50 nsec square-wave pulses (100 pps) from a strip-line pulser (SKL 503A) with a fall time of less than 2 nsec. Minority carrier injection into the (p)GaAs (or GaAsSb) layers was low

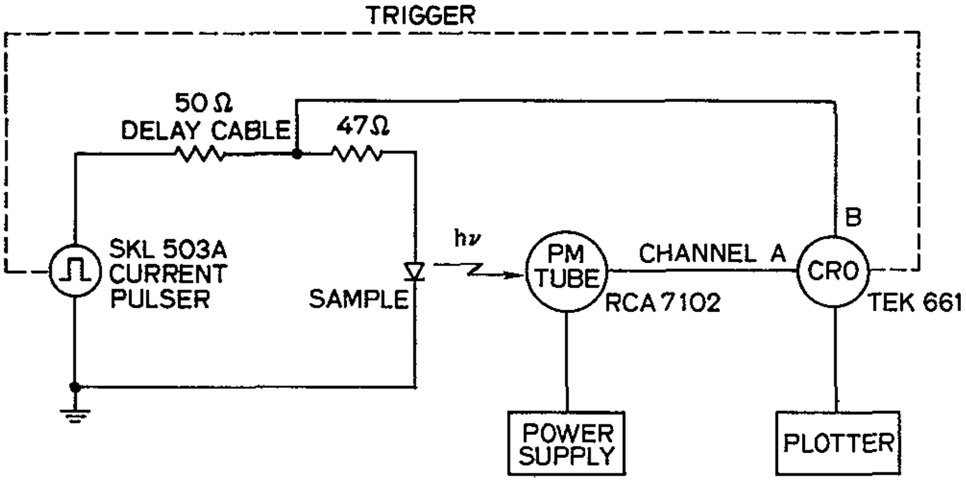

Fig. 23. DIAGRAM OF APPARATUS EMPLOYED TO OBTAIN EL TIME-DECAY LIFETIME MEASUREMENTS ON DH DIODES.

because of the small carrier concentration ($\lesssim 10^{17}/\mathrm{cm}^3$) in the (n)AlGaAs layers. To detect very weak spontaneous EL output signals, the device was placed directly against an RCA 7102 photomultiplier (PM) tube which had an approximately 2.2 nsec response time.

The detected light pulse was displayed and plotted simultaneously on a sampling oscilloscope (Tektronix 661) having less than a 1 nsec response time and on an X-Y recorder (Beckman 1005-02) that produced either linear or log plots of the signals from the oscilloscope output. Figure 24 is a series of linear plots of the detected EL light output pulses from (100)-oriented p-p-n $Al_{0.85}Ga_{0.15}As$-$GaAs_{0.985}Sb_{0.015}$ DH diodes with zero mismatch.

At least three samples for each value of heterojunction spacing d were used to measure the decay times which were determined in the linear portions of the log plots. The results obtained from $Al_{0.85}Ga_{0.15}As$-$GaAs_{1-y}Sb_y$ DH samples are tabulated in Table 6 where, although the measured decay times were slightly scattered (± 0.5 nsec) in each group, the shortest values are listed. A few samples did not reveal a single exponential decay constant (confirmed by the log plots), which may be the result of traps introduced during crystal growth. Bulk lifetime of the minority carriers [6,7,14] was determined from homojunction diodes with thick (~20 μm) p-type GaAsSb layers, using the same technique as described above. In a $GaAs_{0.985}Sb_{0.015}$:Ge layer, $\tau_o = 11$ nsec and $L_n = 1.5$ μm were measured. These are independent parameters used in the analysis to establish recombination velocity at the $Al_{0.85}Ga_{0.15}As$-$GaAs_{1-y}Sb_y$ interfaces. In the AlGaAs-GaAs system, $\tau_o = 31$ nsec and $L_n = 12$ μm were used [6] in the evaluation of interface recombination velocities.

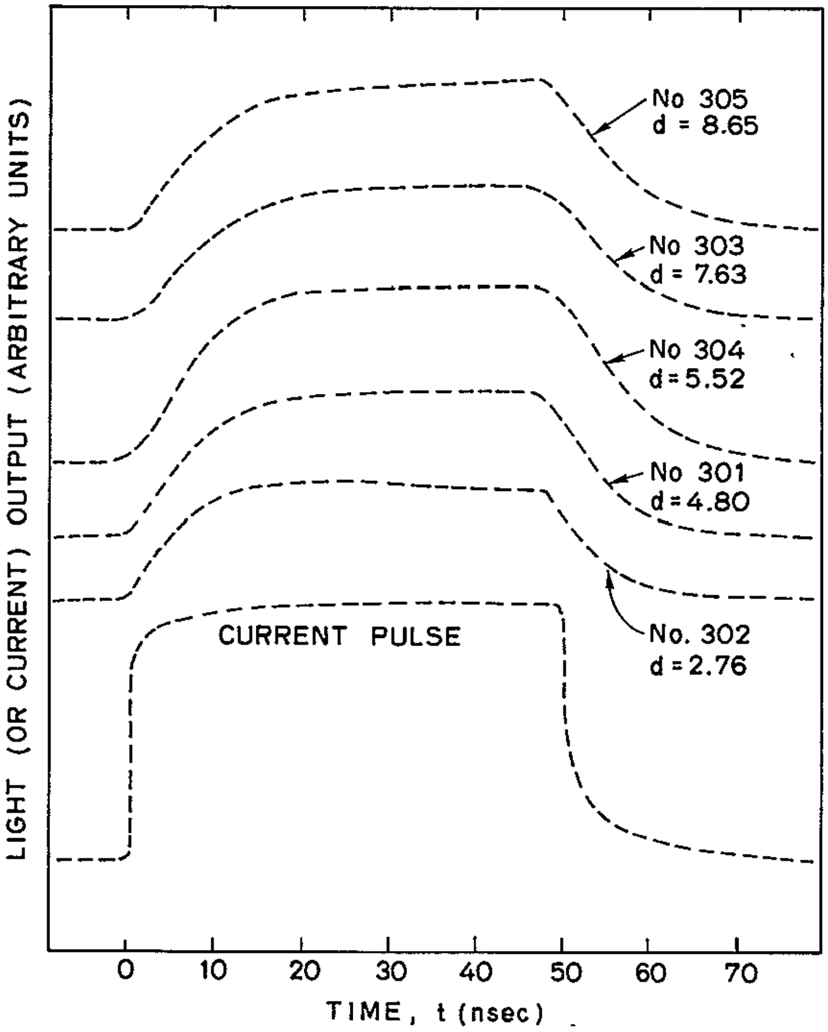

Fig. 24. LINEAR PLOTS OF DETECTED EL LIGHT OUTPUT PULSES FROM (100)-ORIENTED $Al_{0.85}Ga_{0.15}As$-$GaAs_{0.985}Sb_{0.015}$ DH DIODES. A 50-nsec square-wave current pulse was used for excitation. The independent variable is GaAsSb thickness d (μm).

Figure 25 plots the normalized minority carrier lifetime vs the normalized heterojunction spacing, with reduced interface recombination velocity as an independent variable. In the AlGaAs-GaAs system, a comparison of the experimental data to the theoretical curves (Fig. 25a) reveals that $\xi = 0.5$ (equivalent to $S = 2 \times 10^4$ cm/sec) is the best fit for the $Al_{0.85}Ga_{0.15}As$-GaAs DH samples; Ettenberg and Kressel [6] reported

Table 6

HETEROJUNCTION DEVICE PARAMETERS AND LIFETIMES OBTAINED FROM EL TIME-DECAY MEASUREMENTS

Composition and Sample No.	Heterojunction Spacing d (μm)	Measured Electron Lifetime τ_{eff} (nsec)
$Al_{0.85}Ga_{0.15}As-GaAs$		
81-B	2.54	6.36
82-E	6.27	9.83
85-D	10.08	15.90
$Al_{0.85}Ga_{0.15}As-GaAs_{0.985}Sb_{0.015}$		
302	2.76	6.28
301	4.80	5.75
304	5.52	7.30
303	7.63	7.97
305	8.65	8.63
$Al_{0.85}Ga_{0.15}As-GaAs_{0.976}Sb_{0.024}$		
302†	1.44	4.20
301†	4.20	3.98
305†	6.48	5.31

†(111)B GaAs substrate orientation.

that $\xi = 0.1$ (equivalent to $S = 4 \times 10^3$ cm/sec) and $\xi = 0.2$ (equivalent to $S = 8 \times 10^3$ cm/sec) for $Al_{0.25}Ga_{0.75}As-GaAs$ and the $Al_{0.50}Ga_{0.50}As-GaAs$ DH samples, respectively. It is interesting to note that, recently, $S = 3 \times 10^4$ cm/sec was reported [7] for an $In_{0.5}Ga_{0.5}P-GaAs$ interface (0.11 percent mismatch).

In lattice-matched (100)- and (111)B-oriented $Al_{0.85}Ga_{0.15}As-GaAs_{1-y}Sb_y$ systems, $\tau_o = 11$ nsec and $L_n = 1.5$ μm served as the basis for our

ORIGINAL PAGE IS
OF POOR QUALITY

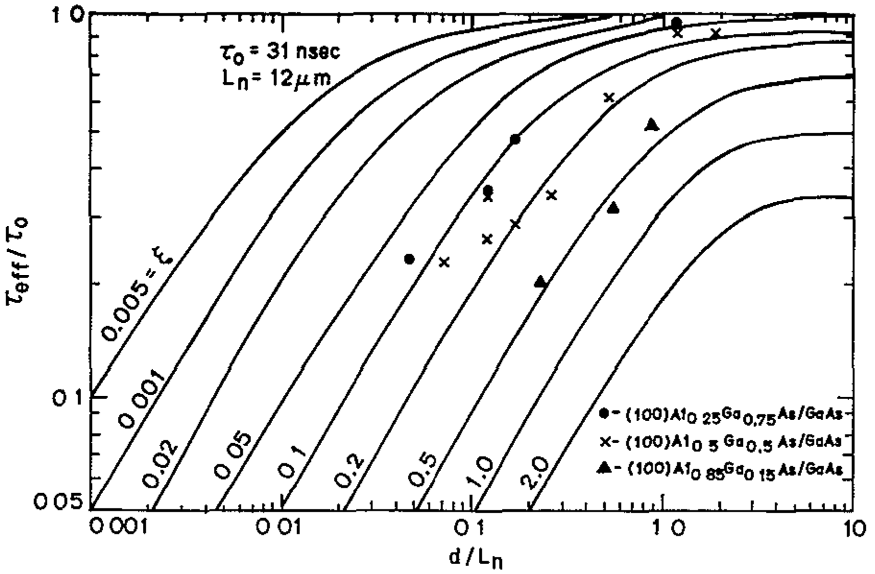

a. AlGaAs-GaAs system

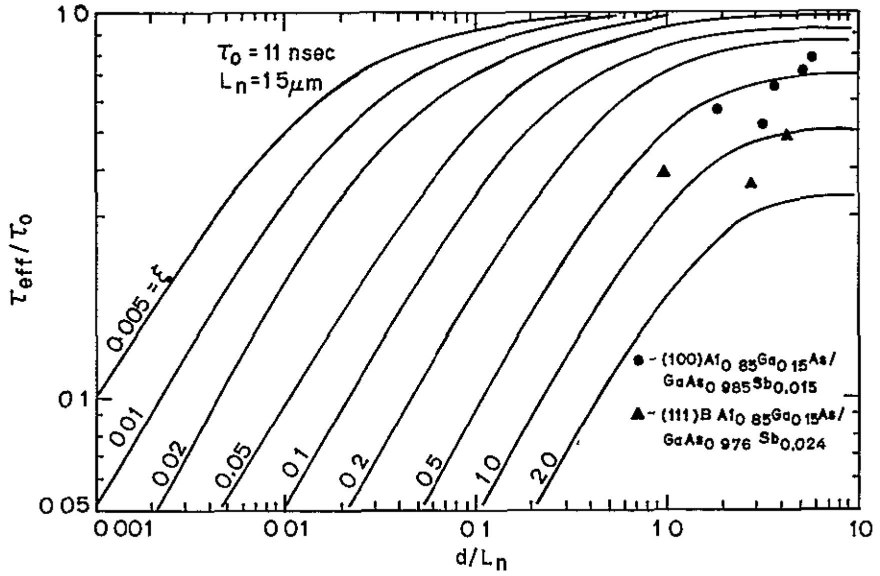

b. $Al_{0.85}Ga_{0.15}As$-GaAsSb system

Fig. 25. NORMALIZED MINORITY CARRIER LIFETIME τ_{eff}/τ_o AS A FUNCTION OF NORMALIZED HETEROJUNCTION SPACING d/L_n. The independent variable is reduced interface recombination velocity $\xi = SL_n/D_n$.

evaluation of interface recombination velocity. The best fits for the (100)-oriented $Al_{0.85}Ga_{0.15}As-GaAs_{0.985}Sb_{0.015}$ and the (111)B-oriented $Al_{0.85}Ga_{0.15}As-GaAs_{0.976}Sb_{0.024}$ DH samples were determined to be $\xi = 0.5$ (equivalent to $S = 7 \times 10^3$ cm/sec) and $\xi = 1.0$ (equivalent to $S = 1.4 \times 10^4$ cm/sec), respectively.

B. Optical Phase Shift

1. Curve-Fitting Techniques

Effective minority carrier lifetime can be indirectly determined from optical phase-shift measurements. When the sample is excited by a pulsed laser, the PL output P [14] is

$$P = \frac{C}{(1 + j\omega\tau_{eff}) + \xi(1 + j\omega\tau_{eff})^{1/2}} = C' e^{-j\theta} \tag{5.1}$$

where C, C' are real quantities, ω is the angular frequency of the pulsed laser, and θ is the phase difference (or phase shift). The phase difference θ between the fundamental Fourier component of the scattered laser and PL output of the sample was directly measured by this technique.

To achieve a more perceptive insight into the curve-fitting technique described above, the following mathematical transformation was made:

$$1 + j\omega\tau_{eff} = \left(1 + \omega^2\tau_{eff}^2\right)^{1/2} e^{j \tan^{-1} \omega\tau_{eff}} \tag{5.2}$$

From the denominator of Eq. (5.1), therefore, $\tan\theta$ is defined as

ORIGINAL PAGE IS
OF POOR QUALITY

$$\tan\theta = \frac{\omega\tau_{eff} + \xi\left(1 + \omega^2\tau_{eff}^2\right)^{1/4} \sin\left(1/2 \tan^{-1} \omega\tau_{eff}\right)}{1 + \xi\left(1 + \omega^2\tau_{eff}^2\right)^{1/4} \cos\left(1/2 \tan^{-1} \omega\tau_{eff}\right)} \qquad (5.3)$$

where, from Eqs. (2.4) and (5.3), $\tan\theta$ is evaluated as a function of S, d, τ_o, and L_n; in Fig. 26, $\tau_o = 16$ nsec and $L_n = 8.9$ μm are the fixed variables. As demonstrated in Chapter II, for given values of τ_o

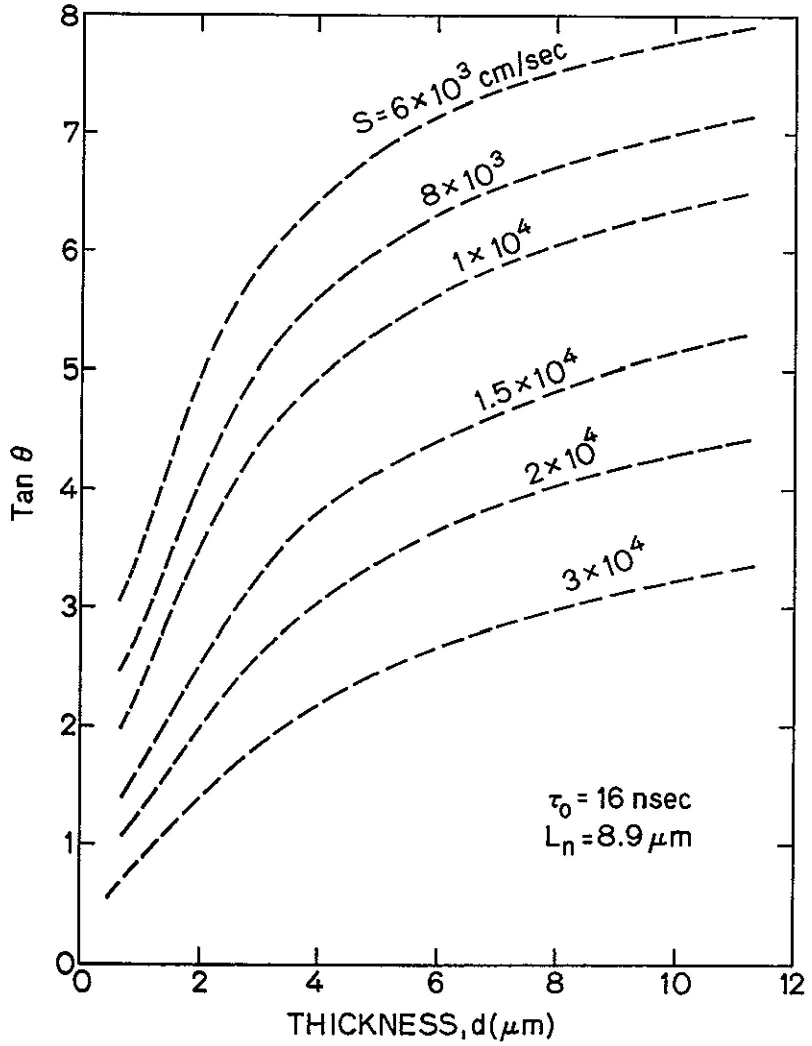

Fig. 26. DETERMINATION OF THE INTERFACE RECOMBINATION VELOCITY BY CURVE FITTING OF OPTICAL PHASE-SHIFT DATA.

and L_n, the interface recombination velocity S is determined by curve fitting from the measured values of d and θ. It can be seen in Fig. 26, that $\tan\theta$ decreases with decreasing d and increasing S; it also increases with increasing τ_o. When τ_o is varied from 13 to 28 nsec, there is little difference in $\tan\theta$ when $d < 10$ μm which indicates that τ_o is not critical at certain ranges when determining S. In addition, when τ_o is smaller than 1 nsec, the curves for different values of S are very closely located. As a result, this type of analysis is inadequate for the evaluation of interface recombination velocity. Similar curve-fitting techniques have been used by Hopkins [9].

2. Phase-Shift Measurement

Figure 27 is a plot of the intensity modulation of a Kr-ion laser beam (Coherent Radiation, Inc., 500K) obtained by a mode-locker (Coherent Radiation, Inc., 465) and included is a diagram of the equipment employed in optical phase-shift measurements. The repetition frequency of the pulsed laser beam was $f \approx 114$ MHz (Fig. 27a), and the average power was $P_{avg} = 50$ mW. The sample was excited by the 6471 Å laser line. The penetration depth in GaAs and GaAsSb layers was ~1/4 μm. A small part of the laser beam was detected by a Si avalanche photodetector after it had been separated from the main beam by a splitter (glass plate) and amplified by an HP 461A. After passing through a band-pass filter, it was used as a reference signal (channel A) of the vector voltmeter (HP 8405A). The PL output of the sample was detected by a photomultiplier (RCA C31024A or RCA 7102) after passing through a grating spectrometer (SPEX 1672 Double-Mate) with a 5 Å resolution (0.25 mm slit width) and was then directed to the signal channel of the vector

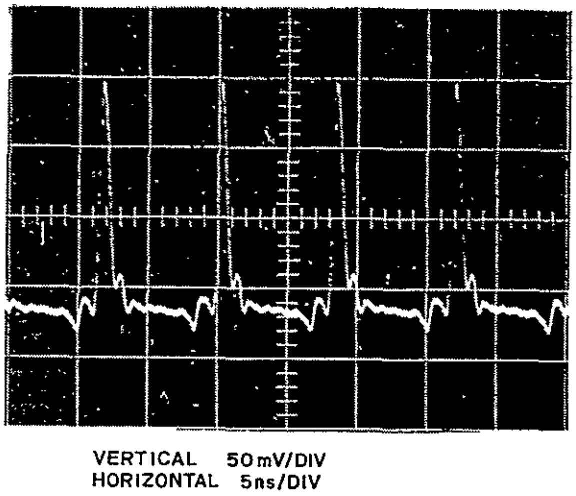

a. Intensity modulation of a Kr-ion laser beam

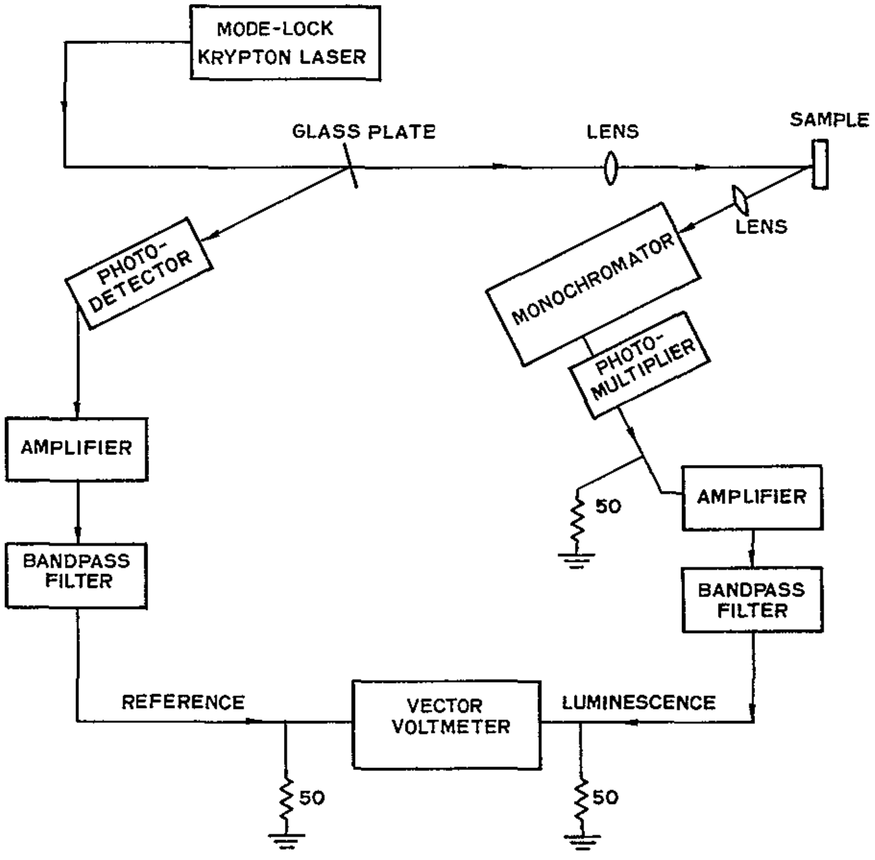

b. Equipment

Fig. 27. OPTICAL PHASE-SHIFT MEASUREMENTS.

voltmeter through an amplifier (HP 462A) and a bandpass filter. The difference in phase between the photoexcitation and PL output of the sample is measured by the vector voltmeter which can also measure absolute signal amplitudes on both channels. The phase difference between the scattered excitation signal and the reference-channel signal establishes a "zero" phase difference. The phase shifts were measured at the PL peaks that had been produced from band-to-band transitions.

In this study, the phase shifts (or radiative lifetimes) were obtained at a sufficiently low excitation level for the hole concentration to equal approximately its equilibrium value so as to ensure that the bulk lifetime is constant. Such measurements were made at room temperature, and the results (namely, $\tan\theta$) are listed in Table 7. It was also observed that the short wavelength PL output $(>E_g)$ had smaller phase shifts (shorter radiative lifetimes) and that the long wavelength PL output $(<E_g)$ had larger phase shifts (longer radiative lifetimes).

Figure 28 plots $\tan\theta$ vs d from the data in Table 7. In the AlGaAs-GaAs system, $\tau_o = 16$ nsec was measured by the same optical phase-shift technique. Curve fitting the experimental data with the theoretical curves (see Fig. 28a) indicates that $S = 3\times10^4$ cm/sec and $L_n = 8.9$ µm are the best fits at an $Al_{0.85}Ga_{0.15}As$-GaAs interface. Although a different value of τ_o was used in the previous curve-fitting analyses of the EL time-decay data, the two measuring techniques (EL time decay and optical phase shift) produce similar results. The different values of τ_o may stem from the fact that EL is an electrical injection mode and PL is an optical injection mode; however, τ_o is not critical at certain ranges when determining S (see Section B.1). The effective lifetime of sample DH-35 was measured at both 300 and 77 K, and it was

Table G-1

Comparative Costs of Alternative Dam Inventory Techniques

ELLTAB

Data Acquisition	\$3600	=	18 x \$200 @ frame
Classification	\$ 315	=	9 x \$ 35 @ frame
Control	\$ 450	=	9 x \$ 50 @ frame
Correction	\$ 900	=	9 x \$100 @ frame
Personnel	\$1000	=	6 man months
	\$6265		
Output	500		
	\$6765		

MANUAL OPTION

Data Acquisition	\$5200	=	10% of area of state @ $\$.14/\text{km}^2$
Compilation	\$8950	=	10% of area of state @ $\$.24/\text{km}^2$
Registration, and Mosaicking	\$9300	=	10% of area of state @ $\$.25/\text{km}^2$
	\$23450		

Table 7

HETEROJUNCTION DEVICE PARAMETERS FOR OPTICAL PHASE SHIFT

Composition and Sample No.	Heterojunction Spacing d (μm)	Phase-Shift tan θ
$Al_{0.85}Ga_{0.15}As$-GaAs		
39	3.2	1.78 to 2.18
42	5.0	2.00 to 2.78
37	5.7	2.37 to 2.92
35	6.6	2.20 to 3.06
40	8.0	2.79 to 3.33
38	9.0	2.69 to 3.19
$Al_{0.85}Ga_{0.15}As$-$GaAs_{0.985}Sb_{0.015}$		
210	1.12	1.73 to 1.80
213	3.84	4.33 to 4.70
207	5.52	5.67 to 6.31
212	6.00	4.92 to 5.14
211	6.96	5.14 to 5.67
208	9.61	5.14 to 5.67
209	11.89	5.67 to 6.31
$Al_{0.85}Ga_{0.15}As$-$GaAs_{0.983}Sb_{0.017}$		
135B[†]	2.16	2.36 to 2.75
133B[†]	2.28	3.27 to 3.73
135A[†]	2.35	3.49 to 4.01
134A[†]	3.00	3.73 to 4.33
133A[†]	3.60	3.73 to 4.70
$Al_{0.85}Ga_{0.15}As$-$GaAs_{0.976}Sb_{0.024}$		
213[†]	2.40	2.05 to 2.14
207[†]	2.74	1.33 to 1.38
211[†]	4.80	2.36 to 2.48
208[†]	5.88	2.25 to 2.36
209[†]	7.80	2.48 to 2.61

[†] (111)B GaAs substrate orientation.

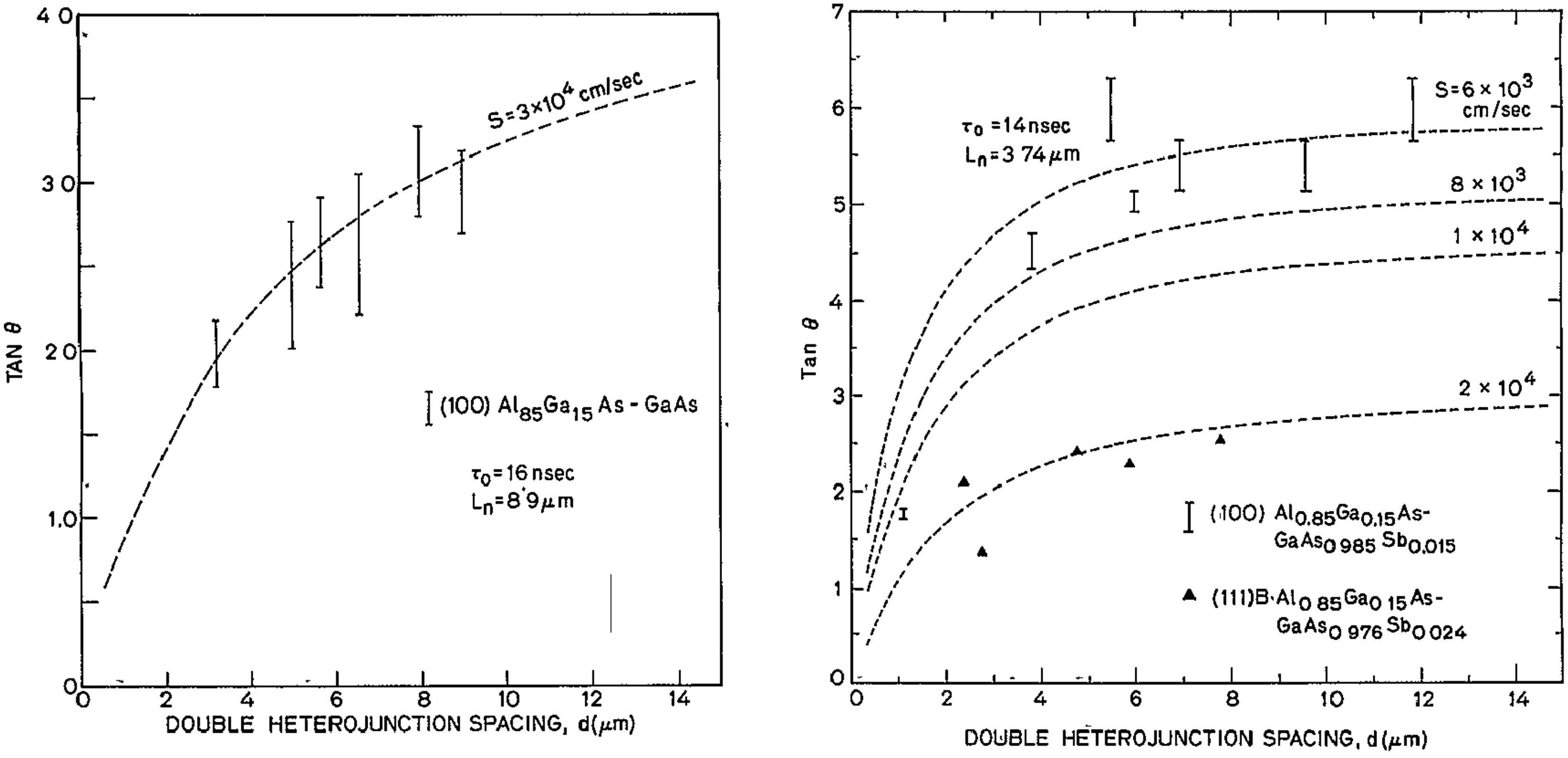

a. AlGaAs-GaAs system

b. AlGaAs-GaAsSb system

Fig. 28. DETERMINATION OF INTERFACE RECOMBINATION VELOCITY BY CURVE FITTING OF THE OPTICAL PHASE-SHIFT DATA. Data taken at 300 K.

observed that its lifetime increased from 3.6 nsec at 300 K to 23.4 nsec at 77 K.

In lattice-matched (100)- and (111)B-oriented $Al_{0.85}Ga_{0.15}As$-$GaAs_{1-y}Sb_y$ systems (Fig. 28b), τ_o = 14 nsec was measured. The best fits are $S = 6 \times 10^3$ and 2×10^4 cm/sec with L_n = 3.74 μm at the (100)-oriented $Al_{0.85}Ga_{0.15}As$-$GaAs_{0.985}Sb_{0.015}$ and (111)B-oriented $Al_{0.85}Ga_{0.15}As$-$GaAs_{0.976}Sb_{0.024}$ interfaces, respectively.

C. Discussion

Figure 29 summarizes the measured values of interface recombination velocity as a function of strain-free lattice mismatch at room temperature. The ● indicates the (100)-oriented $Al_xGa_{1-x}As$-GaAs interface system, and ▲ and ■ denote (100)- and (111)B-oriented $Al_{0.85}Ga_{0.15}As$-$GaAs_{1-y}Sb_y$ interface systems, respectively. In addition, ○ designates optical phase-shift measurements, whereas the remaining points specify EL time-decay measurements. In the AlGaAs-GaAs system, the points at 0.038 percent (x = 0.25) and 0.075 percent (x = 0.50) mismatch are those reported by Ettenberg [6] of RCA, and the ones at 0.126 percent (x = 0.85) mismatch are the results obtained from this analysis. Note an exponential relationship between interface recombination velocity and lattice mismatch.

The addition of 1.5 percent Sb to (100)-oriented GaAs produces a near-zero mismatch in $Al_{0.85}Ga_{0.15}As$ and lowers the interface recombination velocity from (2 to 3) $\times 10^4$ cm/sec (y = 0) to (6 to 7) $\times 10^3$ cm/sec. Although this value is slightly higher than expected from the linear relationship in the semilog plot, solar cells made from such a combination of materials should have an excellent spectral response at short

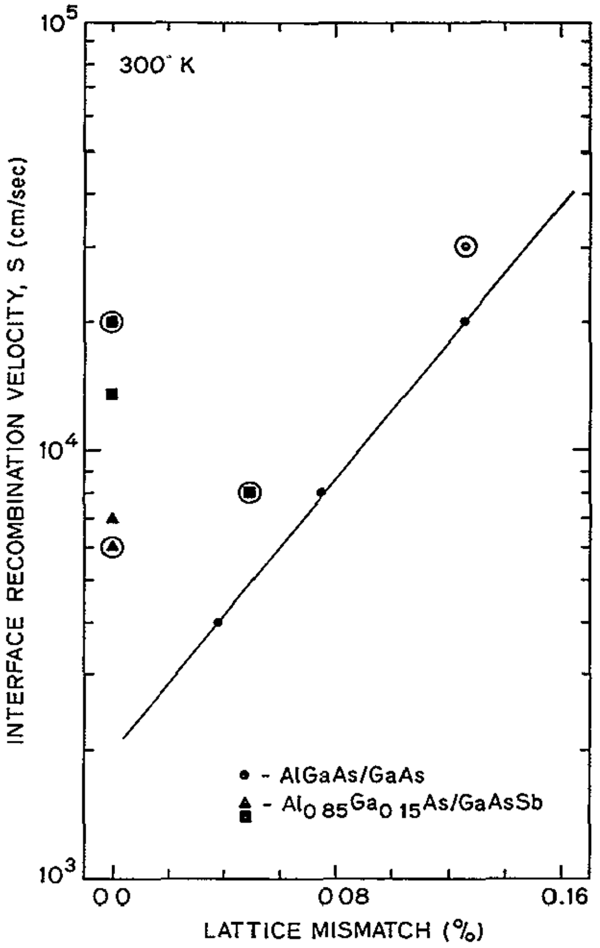

Fig. 29. INTERFACE RECOMBINATION VELOCITY VS LATTICE MISMATCH AT 300 K IN $Al_xGa_{1-x}As$-GaAs AND $Al_{0.85}Ga_{0.15}$ As-$GaAs_{1-y}Sb_y$ DOUBLE HETEROJUNCTIONS. The ●, ▲, ■ are from EL time-decay techniques, and ◉, (▲), (■) are from optical phase-shift techniques.

wavelengths resulting from the large band gap of the $Al_{0.85}Ga_{0.15}As$ window material (E_g = 2.05 eV) and at long wavelengths because of the addition of Sb to the GaAs active layer. Theoretical studies [20,47] indicate that, when the interface recombination velocity becomes less than 10^4 cm/sec, further reduction in S does not improve the solar-cell spectral response. The lattice-matched AlGaAs-GaAsSb solar cells developed in this research, therefore, are nearly ideal in this respect.

Similar measurements on a lattice-matched (111)B-oriented $Al_{0.85}Ga_{0.15}As-GaAs_{0.976}Sb_{0.024}$ interface resulted in $S = (1.4 \text{ to } 2) \times 10^4$ cm/sec, and $S = 9 \times 10^3$ cm/sec was obtained at a (111)B-oriented $Al_{0.85}Ga_{0.15}As-GaAs_{0.983}Sb_{0.017}$ interface (~0.048 percent mismatch at 300 K). Both samples revealed elastic lattice deformation without misfit dislocations.

Ettenberg [8] obtained $S = 2.5 \times 10^4$ and 3×10^4 cm/sec at $In_{0.503}Ga_{0.497}P-GaAs$ (~0.14 percent mismatch at 300 K) and $In_{0.491}Ga_{0.509}P-GaAs$ (~0.048 percent mismatch at 300 K) heterojunction interfaces, respectively. Both samples displayed only elastic lattice deformation. The $In_{0.491}Ga_{0.509}P-GaAs$ interface had approximately the same recombination velocity as that of our $Al_{0.85}Ga_{0.15}As-GaAs$ interface although the former had a much smaller lattice mismatch at 300 K. Ettenberg concluded that, when the lattice constant of epitaxial layers was larger than the underlying substrate, the interface recombination velocity varies linearly as a function of growth-temperature lattice mismatch resulting in misfit dislocations; however, there were no misfit dislocations in the above InGaP-GaAs samples.

Chapter VI

CONCLUSIONS AND RECOMMENDATIONS

A. Conclusions

The interface recombination velocity as a function of lattice mismatch at $Al_xGa_{1-x}As$-GaAs (or $GaAs_{1-y}Sb_y$) heterojunction interfaces was investigated. P-p-p and p-p-n DH samples were prepared on (100)- and (111)B-oriented boat-grown (n)GaAs:Te substrates, using a horizontal sliding boat LPE growth system. The values of x and y were controlled by adding known amounts of Al or Sb to As-saturated Ga melts. Auger analyses in addition to Al or Sb concentration microprobe line profiles and PL spectra revealed that the DH samples had nearly abrupt heterojunctions and that there was no perceptible cross diffusion of Al or Sb at the interfaces.

A method was developed to determine the lattice mismatch and the lattice constants in mixed single crystals. When heteroepitaxial layers were grown, either elastic lattice deformation or misfit dislocations were observed because of the differences in the lattice constants and thermal expansion coefficients. An effective Poisson ratio was applied to the elastic lattice-deformation condition to detect the strain-free lattice mismatch from the strained lattice mismatch; in misfit dislocations, the strain-free lattice mismatch was obtained directly from X-ray diffraction profiles rather than from the Poisson ratio. From precise measurements of AlGaAs single layers grown on GaAs substrates, ν_{eff} = 0.312 and 0.190 were observed in (100)- and (111)B-oriented AlGaAs layers, respectively. No ν_{eff} was involved in the (100)-oriented GaAsSb layers although $\nu_{eff} = 0.190$ was chosen for the (111)B-oriented GaAsSb layers.

Assuming that a_o(GaAs) = 5.6532 Å resulted in $a_o(Al_xGa_{1-x}As) = 5.6532 + 0.0084x$ Å which is in good agreement with Vegard's law. Lattice-matched $Al_{0.85}Ga_{0.15}As-GaAs_{1-y}Sb_y$ layers were grown on both (100)- and (111)B-oriented GaAs substrates at a ratio of $W_{Sb}/W_{Ga} = 0.13$ and a temperature of 840 to 820°C although the corresponding Sb compositions were different ($y = 0.015$ and 0.024) because of the dependence of the Sb distribution coefficient on substrate orientation. When a_o(GaSb) = 6.0959 Å was assumed at 300 K, both (100)- and (111)B-oriented GaAsSb layers deviated only slightly from Vegard's law.

Interface recombination velocity in the $Al_{0.85}Ga_{0.15}As-GaAs_{1-y}Sb_y$ system was determined from the dependence of the effective minority carrier lifetime on double-heterojunction spacing, using both optical phase shift and EL time decay, and good agreement between these recombination velocities was obtained by the two techniques. The addition of 1.5 percent Sb to (100)-oriented GaAs produces a near-zero mismatch with $Al_{0.85}Ga_{0.15}As$ and lowers the velocity from $(2 \text{ to } 3) \times 10^4$ ($y = 0$) to $(6 \text{ to } 7) \times 10^3$ cm/sec. Lattice-matched (100)-oriented $Al_{0.85}Ga_{0.15}As-GaAs_{0.985}Sb_{0.015}$ solar cells have sufficiently low values of S to make them nearly ideal devices. They should have an excellent spectral response to photons with energies over the full range from 1.4 to 2.6 eV.

B. Recommendations

The recombination velocities at $Al_{0.85}Ga_{0.15}As-GaAs_{1-y}Sb_y$ heterojunction interfaces were measured only at room temperature. An exponential relationship between interface recombination velocity and lattice mismatch was observed in the AlGaAs-GaAs system; however, these velocities deviated at $Al_{0.85}Ga_{0.15}As-GaAs_{1-y}Sb_y$ interfaces. As a result, thermal expansion coefficient measurements of these ternary materials should be conducted over the range from room to growth temperatures so as to determine the general relationship between interface recombination velocity and lattice mismatch in systems based on different materials. The analysis should include a quantitative evaluation of the contributions of misfit dislocations and elastic strain to recombination velocity. The measurements should also extend to AlGaAsP-GaAs interfaces. The information obtained from all of these measurements can then be used to optimize the performance of heterojunction solar cells and other devices such as light-emitting diodes and laser diodes.

This investigation has demonstrated that the recombination velocity at a $Al_{0.85}Ga_{0.15}As$-$GaAs_{0.985}Sb_{0.015}$ lattice-matched heterojunction is sufficiently small for maximum solar-cell collection efficiency. This result should be tested by constructing working models of (p)$Al_{0.85}Ga_{0.15}As$-(p)$GaAs_{0.985}Sb_{0.015}$-(n)GaAs solar-cell structures. The spectral response, short-circuit current, fill factor, and conversion efficiency should be examined under terrestrial sunlight conditions and compared to conventional AlGaAs-GaAs solar cells.

Appendix

ELASTIC DEFORMATION OF CUBIC LATTICE AND RELATED ELASTIC CONSTANTS [48]

Two-Dimensional Case: $\sigma^{\perp} = 0$

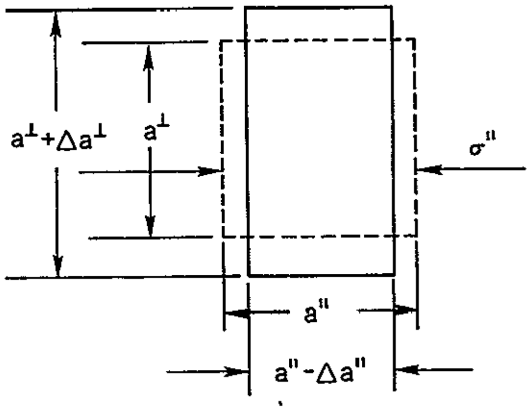

<u>Definition</u>

$E = \sigma^{\parallel}/\epsilon^{\parallel}$

$\nu = -\epsilon^{\perp}/\epsilon^{\parallel}$

then,

$\epsilon^{\parallel} = (1/E)\ \sigma^{\parallel}$

$\epsilon^{\perp} = (-\nu/E)\ \sigma^{\parallel}$

Three-Dimensional Case: $\sigma_{zz} = 0$ <u>and</u> $\sigma_{xx} = \sigma_{yy} = \sigma$

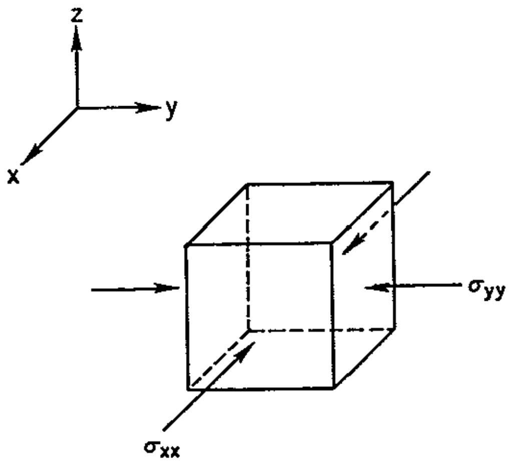

$$\begin{aligned} \epsilon_{xx} &= \epsilon_{yy} \\ &= \epsilon^{\parallel} + \epsilon^{\perp} \\ &= (1-\nu/E)\ \sigma^{\parallel} \\ \epsilon_{zz} &= 2\epsilon^{\perp} \\ &= (-2\nu/E)\ \sigma^{\parallel} \\ &= (-2\nu/1-\nu)\ \epsilon_{xx} \end{aligned}$$

REFERENCES

1. J. J. Loferski, 25th Annual Proc. Power Sources Conf. (May 1972), pp. 1-4.

2. H. Fischer, FESTKÖRPERPROBLEME XIV Advances in Solid State Physics, Edited by H. J. Queisser, Stuttgart (Pergamon-Vieweg, 1974), pp. 153-182.

3. L. W. James and R. L. Moon, Appl. Phys. Lett. 26, 476 (1975).

4. H. C. Casey, Jr. and F. A. Trumbore, Mat. Sci. and Eng. 6, 69 (1970).

5. A. Many, Y. Goldstein, and N. B. Grover, Semiconductor Surfaces (North-Holland, Amsterdam, 1965).

6. M. Ettenberg and H. Kressel, J. Appl. Phys. 47, 1538 (1976).

7. M. Ettenberg, C. J. Nuese, and G. H. Olsen, J. Appl. Phys. 48, 1288 (1977).

8. M. Ettenberg and G. H. Olsen, J. Appl. Phys. 48, 4275 (1977).

9. R. H. Hopkins, J. R. Davis, P. Rai-Choudhury, P. D. Blais, and J. R. McCormick, "Silicon Materials Task of the Low Cost Solar Array Project (Part 2)," Second Quarterly Report, 1 January-31 March 1976, Westinghouse Research Laboratories, p. 43.

10. E. M. Pell, Phys. Rev. 90, 278 (1953).

11. R. H. Dean and C. J. Nuese, IEEE Trans. ED-18, 151 (1971).

12. G. A. Acket, W. Nijman, R. P. Tijburg, and P. J. de Waard, GaAs and Related Compounds, Inst. Phys. Conf. Ser. No. 24, 181 (1975).

13. D. L. Keune, N. Holonyak, Jr., R. D. Burnham, D. R. Scifres, and H. R. Zwicker, J. Appl. Phys. 42, 2048 (1971).

14. G. A. Acket, W. Nijman, and H. 't Lam, J. Appl. Phys. 45, 3033 (1974).

15. D. T. Cheung, "Properties of III-V Compound Heterojunctions Prepared by Liquid Phase Epitaxial Techniques," Ph.D. dissertation, SEL-75-013, Stanford University, Stanford, Calif. (1975), p. 12.

16. M. B. Panish, J. Appl. Phys. 44, 2659 (1973).

17. J. Vilms and J. P. Garrett, Solid State Electronics 15, 443 (1972).

18. A. J. SpringThorpe, F. D. King, and A. Becke, J. Elect. Mat. 4, 101 (1975).

19. K. K. Shih and G. D. Pettit, J. Elect. Mat. 3, 391 (1974).

20. L. C.-C. Shen, "Preparation and Properties of Grown Junction GaAs Solar Cells," Ph.D. dissertation, SEL-76-020, Stanford University, Stanford, Calif. (1976), p. 40.

21. T. Y. Wu and G. L. Pearson, J. Phys. Chem. Solids 33, 409 (1972).

22. G. A. Antypas, J. Electrochem. Soc. 117, 1393 (1970).

23. M. Kurihara, T. Moriizumi, and K. Takahashi, Solid State Electronics 16, 763 (1973).

24. M. Ettenberg and H. F. Lockwood, GaAs and Related Compounds, Inst. Phys. Conf. Ser. No. 24, 102 (1975).

25. D. Huber and W. Gramman, GaAs and Related Compounds, Inst. Phys. Conf. Ser. No. 24, 223 (1975).

26. M. Ettenberg, C. J. Nuese, J. R. Appert, J. J. Gannon, and R. E. Enstrom, J. Elect. Mat. 4, 37 (1975).

27. B. Schwartz, J. C. Dyment, and S. E. Haszko, GaAs and Related Compounds, Inst. Phys. Conf. Ser. No. 17, 187 (1973).

28. R. A. Logan and F. K. Reinhart, J. Appl. Phys. 44, 4172 (1973).

29. F. E. Rosztoczy, F. Ermanis, I. Hayashi, and B. Schwartz, J. Appl. Phys. 41, 264 (1970).

30. A. G. Milnes, Deep Impurities in Semiconductors, Wiley-Interscience (1973), p. 47.

31. C. M. Garner, Y. D. Shen, J. S. Kim, G. L. Pearson, W. E. Spicer, J. S. Harris, and D. D. Edwall, J. Appl. Phys. 48, 3147 (1977).

32. C. M. Garner, Y. D. Shen, J. S. Kim, G. L. Pearson, W. E. Spicer, J. S. Harris, D. D. Edwall, and R. Sahai, J. Vac. Sci. Technol. 14, 985 (1977).

33. L. Jastrzebski, J. Lagowski, and H. C. Gatos, Appl. Phys. Lett. 27, 537 (1975).

34. A. M. Sekela, D. L. Feucht, and A. G. Miles, GaAs and Related Compounds, Inst. Phys. Conf. Ser. No. 24, 245 (1975).

35. G. A. Rozgonyi, P. M. Petroff, and M. B. Panish, J. Cryst. Growth 27, 106 (1974).

36. S. Kishino, M. Ogirima, T. Kajimura, and K. Kurata, J. Cryst. Growth 24/25, 266 (1974).

37. S. Isomae, S. Kishino, and M. Takahashi, J. Cryst. Growth 23, 253 (1974).

38. E. Estop, A. Izrael, and M. Sauvage, Acta Cryst. A32, 627 (1976).

39. T. Hattanda and A. Takeda, Japan J. Appl. Phys. 12, 1104 (1973).

40. K. Ishida, J. Matsui, T. Kamejima, and L. Sakuma, Phys. Stat. Sol. (a) 31, 255 (1975).

41. C. Schiller, GaAs and Related Compounds, Inst. Phys. Conf. Ser. No. 33a, 25 (1977).

42. W. A. Brantley, J. Appl. Phys. 44, 534 (1973).

43. H. Nagai, J. Appl. Phys. 45, 3789 (1974).

44. I. Kudman and R. J. Paff, J. Appl. Phys. 43, 3760 (1972).

45. M. Ettenberg and R. J. Paff, J. Appl. Phys. 41, 3926 (1970).

46. J. C. Woolley, J. Electrochem. Soc. 112, 461 (1965).

47. J. M. Woodall and H. J. Hovel, Appl. Phys. Lett. 21, 379 (1972).

48. H. W. Hayden, W. G. Moffatt, and J. Wulff, The Structure and Properties of Materials, Vol. III (Mechanical Behavior) (John Wiley & Sons, Inc., N.Y., 1965), p. 24.